JOURNAL OF GEOPHYSICAL RESEARCH, VOL. 106, NO. D23, PAGES 31,755–31,770, DECEMBER 16, 2001

Error analysis and characterization of atmospheric profiles retrieved from GNSS occultation data

Markus J. Rieder and Gottfried Kirchengast

Institute for Geophysics, Astrophysics, and Meteorology (IGAM), University of Graz, Graz, Austria

Abstract. The performance of the Global Navigation Satellite System (GNSS) based radio occultation method for providing retrievals of atmospheric profiles up to the mesosphere was investigated by a rigorous Bayesian error analysis and characterization formalism. Starting with excess phase profile errors modeled as white Gaussian measurement noise, covariance matrices for the retrieved bending angle, refractivity/density, pressure, and temperature profiles were derived in order to quantify the accuracy of the method and to elucidate the propagation of statistical errors through subsequent steps of the retrieval process. We assumed unbiased phase errors (the occultation method is essentially self-calibrating), spherical symmetry in the occultation tangent point region (reasonable for most atmospheric locations), and dry air (disregarding humidity being of relevance below 10 km in the troposphere only) in this baseline analysis. Because of the low signal-to-noise ratio of occultation data at mesospheric heights, which causes instabilities in case of direct inversion from excess phase profiles to atmospheric profiles, a Bayesian approach was employed, objectively combining measured data with a priori data. For characterization of the retrievals we provide, in addition to covariance estimates for the retrieved profiles, quantification of the relationship between the measured data, the retrieved state, the a priori data, and the true state, respectively. Averaging kernel functions, indicating the sensitivity of the retrieval to the true state, contribution functions, indicating the sensitivity of the retrieval to the measurement, and the ratio of retrieval errors to a priori errors are shown. Two different sensor scenarios are discussed, respectively, an advanced receiver (AR) scenario with 2 mm and a standard receiver (SR) scenario with 5 mm unbiased RMS error on excess phase data at 10 Hz sampling rate. The corresponding bending angle, refractivity, pressure, and temperature retrieval properties are shown. Temperature, the final data product, is found to be accurate to better than 1 K below ~40 km (AR)/~35 km (SR) at ~2 km height resolution and to be dominated by a priori knowledge above ~55 km (AR)/~47 km (SR), respectively. For all data products the use of a Bayesian framework allowed for a more complete and consistent quantification of properties of profiles retrieved from GNSS occultation data than previous work.

1. Introduction

The radio occultation technique exploits Global Navigation Satellite System (GNSS) signals, which propagated through the Earth's atmosphere in limb sounding geometry (the GNSS presently comprises the U.S. Global Positioning System, GPS, and its Russian pendant called GLONASS; a European system called GALILEO is under development). The principal observable is the excess phase path (phase path in excess to phase path in vacuum) of GNSS-transmitted radio waves accrued by refraction during their passage through the atmosphere to a receiver in low Earth orbit. Using the excess phase data, profiles of atmospheric bending angle, refractivity, density, pressure, and temperature can be retrieved, which range from surface to mesosphere. In addition, humidity information can be extracted in the lower and middle troposphere. The technique has been described in detail in various papers (e.g., see review by *Kursinski et al.* [1997]) and has been successfully demonstrated with the GPS meteorology (GPS/MET) "proof-of-concept" experiment [*Ware et al.*, 1996; *Kursinski et al.*, 1996]. The GLONASS system has not yet been utilized for an actual experiment.

A variety of data analysis studies based on either simulated data or GPS/MET data or both, which employed forward/inverse simulations as well as validation of GPS/MET data with independent data sets, have confirmed a very good quality of retrieved profiles up to ~30–35 km, such as temperature accuracy ≤1 K (we disregard pending humidity-related problems in tropospheric processing in this study) [e.g., *Rocken et al.*, 1997; *Gorbunov and Gurvich*, 1998; *Steiner et al.*, 1999; *Syndergaard*, 1999; *Palmer et al.*, 2000]. However, they also showed that the low signal-to-noise ratio above the stratopause constitutes a basic limitation of the accuracy of retrieval products above about 35 km. For this reason the measured data have been supported in one way or another by additional model information in those regions, generally by "statistical optimization" combining measured bending angle data with model bending angle data, a concept introduced by *Sokolovskiy and Hunt* [1996].

Paper number 2000JD000052.
0148-0227/01/2000JD000052$09.00

Regarding error analyses, only the recent works by *Syndergaard* [1999] and *Palmer et al.* [2000] have stepped beyond a standard analysis of RMS errors in retrieval products and also considered covariances. *Syndergaard* [1999] performed a theoretical step-by-step covariance propagation analysis from excess phase profiles via intermediate data products such as bending angle and refractivity down to temperature profiles. *Palmer et al.* [2000] performed a theoretical error analysis for a Bayesian optimal estimation inversion of bending angle profiles into temperature profiles, humidity profiles, and surface pressure.

This study complements and extends the work of *Syndergaard* [1999] and *Palmer et al.* [2000] with an error analysis and characterization of atmospheric profiles retrieved from excess phase data utilizing the rigorous Bayesian data analysis framework introduced by *Rodgers* [1976, 1990, 2000]. This concept copes both with the task of optimally supporting the retrieval by measurement-independent model (a priori) data as well as with the task of quantifying expected errors and the relationships between measured data, a priori data, retrieved state, and true state. Such an error analysis and characterization is highly valuable for assessing the reliability of retrieval products and for a solid understanding of retrieval product properties.

This study is organized as follows. In section 2 a critical inspection of the experimental setup, the signal-to-noise ratio, and inversion techniques utilized so far motivate the use of Bayesian data analysis. Section 3 summarizes the Bayesian approach to underdetermined inversion problems and the subsequently employed methodology for error analysis and characterization of a retrieval process. In section 4 the error covariance and characterization matrices quantifying the performance properties of data products are discussed on the basis of two reasonable scenarios of excess phase measurement errors ("advanced," reflecting the performance of a modern receiver, and "standard," reflecting the performance of the GPS/MET proof-of-concept receiver). After describing the formulation of required input quantities in section 4.1, the properties of retrieved bending angle, refractivity/density, pressure, and temperature profiles are assessed successively in sections 4.2 to 4.5. For each retrieval product the covariance structure is analyzed, and RMS errors and error correlation functions are shown and discussed. In addition, the structure of the averaging kernel matrix, the data contribution (or gain) matrix, and the retrieved/a priori error ratio vector are illustrated and discussed for each retrieved profile. Section 5, finally, provides a concise summary and the main conclusions of the study.

2. Measurements and Need for Bayesian Data Analysis

Briefly summarized, GNSS occultation measurements are collected as follows. The transmitting satellite corresponds to an electromagnetic point source of well-defined L band signals, the atmosphere acts like a weak inhomogeneous lens, and the receiving satellite acquires, from the point of view of geometric optics that we adopt here, a Fresnel diffraction-limited signal. The natural vertical resolution thus achieved is <1.5 km in the stratosphere and <0.5 km in the lower troposphere. The horizontal resolution is ~300 km along a ray path and ~1.5 km perpendicular to it. The local bending of occultation rays can be understood by Snell's law linking gradients in the refractivity field of the atmosphere to changes in ray direction. The cumulative effect of the atmosphere along the path of propagation can be characterized by the excess phase l at a given measurement time t and, after a conversion based on the excess Doppler $d = (dl/dt)$, by the total bending angle α associated with an impact parameter a. The phase l is (up to a constant in practice) the total phase path increase (in length units) due to signal retardation and ray bending caused by the atmospheric refractivity field. Assuming local spherical symmetry near ray perigee, a is the perpendicular distance between the center of the local curvature at ray perigee (in the plane transmitter-receiver-Earth center) and the ray asymptote at transmitter or receiver. The parameter α is the (small) opening angle between the transmitter and receiver asymptotes. Detailed descriptions of the measurement principle have been given, for example, by *Melbourne et al.* [1994], *Hoeg et al.* [1995], and *Kursinski et al.* [1997].

A GNSS occultation sensor system as a whole comprises, in terms of total error in "measured" neutral atmospheric excess phase profiles $\mathbf{l}$, a variety of individual error components including as major ones satellite velocity and position errors, residual clock errors, local multipath errors, thermal noise, and residual ionospheric errors. The relative importance of these error components in the total error and the magnitude and statistical characteristics of the total error depend most importantly on technical properties and performance of the sensor system but also on observation geometry and atmospheric and ionospheric conditions. The total excess phase error thus has to be individually estimated for any given specific sensor system in form of an aggregate result of a thorough error budget analysis. A generic analysis of this type, including some proxy error component estimates, has been discussed in the open literature most comprehensively by *Kursinski et al.* [1997].

In this study we do not perform any error budget analysis but rather take two representative scenarios ("advanced receiver," AR, and "standard receiver," SR) of total error in neutral atmospheric excess phase profiles $\mathbf{l}$ as the starting point of an error analysis and characterization formalism, which is targeted at quantifying the errors and properties of retrieved atmospheric profiles given an excess phase profile with errors as specified. Using $\mathbf{l}$ as starting point intrinsically assumes it to be obtained from the original phase measurements at GNSS frequencies L1 and L2 via ionosphere correction by linear combination of phases, while linear combination of bending angles is a superior ionosphere correction method [*Vorob'ev and Krasil'nikova*, 1994; *Ladreiter and Kirchengast*, 1996; *Hocke et al.*, 1997; *Kursinski et al.*, 1997] more frequently used in practice. Our analysis dealing with unbiased statistical errors also applies to the latter method, however, since its superiority essentially lies in improved bias mitigation and since otherwise both the linear combination coefficients and the processing algorithm from phase to bending angle are the same for the two methods. The excess phase errors are introduced in the generic form of a measurement error covariance matrix, $\mathbf{S}_\varepsilon$. The two scenarios discussed in this study can thus be complemented without change to the formalism by any other desired scenario with a different specification of $\mathbf{S}_\varepsilon$.

In previous studies, the problem of low signal-to-noise ratio (SNR) of GNSS occultation data at heights above the stratopause was generally addressed at the level of bending

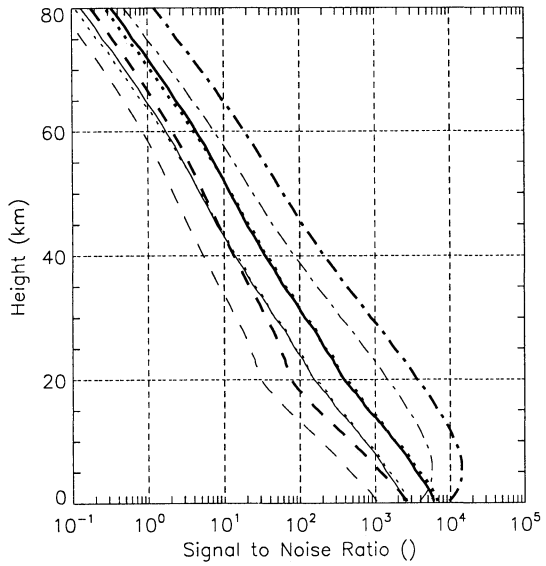

Figure 1. Diagonal of the SNR matrix $\mathbf{S}_\varepsilon^{-1/2} \cdot \mathbf{K} \cdot \mathbf{S}_{ap}^{1/2}$ representing the SNR height profile. Bending angle (dashed-dotted), refractivity (solid), pressure (dotted; closely following the refractivity SNR profile), and temperature (dashed) SNR profiles are shown for both the AR scenario (heavy lines) and the SR scenario (light lines), respectively.

angle data by invoking model data in order to damp instabilities in subsequent retrieval steps, which otherwise would arise due to the low SNR. The stabilization and smoothing have usually been performed in an approximate manner, without fully exploiting the error covariance information of the contributing data sources [*Kursinski et al.*, 1996; *Sokolovskiy and Hunt*, 1996; *Hocke*, 1997; *Rocken et al.*, 1997; *Steiner et al.*, 1999; *Syndergaard*, 1999]. This study avoids potential weaknesses of approximate methods in that we strictly base the whole analysis on the rigorous Bayesian inversion methodology described by *Rodgers* [1976, 1990, 2000], which allows combining measurement data and a priori model data in a statistically optimal manner. Utilizing this methodology we retrieve, given an excess phase profile $\mathbf{l}$ with error covariance $\mathbf{S}_\varepsilon$ as measurement, properties of atmospheric profiles at all levels (bending angle, refractivity, pressure, and temperature) by using a single generic algorithm described as needed for our purpose in section 3. Briefly, the basic ingredient is that the relationship between the desired atmospheric profile $\mathbf{x}$ and the measured profile $\mathbf{l}$, called the forward model, is prepared in an algebraic form, where a forward operator matrix $\mathbf{K}$ maps $\mathbf{x}$ into $\mathbf{l}$. The optimal estimation inversion, the retrieval of $\mathbf{x}$ given $\mathbf{l}$, can then be considered as a combination of information on $\mathbf{x}$ in the measurements $\mathbf{l}$ and in a prescribed a priori profile $\mathbf{x}_{ap}$, the contributions optimally weighted by the measurement error covariance $\mathbf{S}_\varepsilon$ and the a priori error covariance $\mathbf{S}_{ap}$ in the sense of best linear unbiased estimation.

Expecting low SNR in the mesosphere it is apt, before performing the Bayesian analysis, to inquire the effective number of independent measurement values and, in particular, to quantitatively estimate the SNR profile associated with each desired profile $\mathbf{x}$. We thus compared the measurement errors specified by $\mathbf{S}_\varepsilon$ with the natural variability as reflected by the a priori knowledge on $\mathbf{x}$ specified by $\mathbf{S}_{ap}$. Any component of $\mathbf{x}$ whose variability, after mapped into measurement space by the forward operator $\mathbf{K}$, is smaller than the measurement error is in effect not measurable. The number of independent measurement values, detectable to better than measurement error given natural variability, is the number of singular values of matrix $\mathbf{S}_\varepsilon^{-1/2} \cdot \mathbf{K} \cdot \mathbf{S}_{ap}^{1/2}$, which are greater than about unity and its diagonal is an estimate of the SNR profile [*Rodgers*, 2000]. Figure 1 depicts the diagonal of $\mathbf{S}_\varepsilon^{-1/2} \cdot \mathbf{K} \cdot \mathbf{S}_{ap}^{1/2}$ for each of the retrieval products bending angle, refractivity, pressure, and temperature for the two scenarios adopted (the matrices involved and the scenarios are detailed in section 4). The SNR falls back to below unity in the mesosphere for all profiles. The AR scenario maintains a given SNR about one scale height higher up than the SR scenario. The SNR degrades in course of the retrieval process, that is, the bending angle profile exhibits highest SNR, the temperature profile lowest. These aspects of SNR behavior are in line with qualitative expectations and strongly confirm the potential utility of Bayesian optimal estimation for GNSS occultation data analysis.

3. Optimal Estimation Retrieval, Error Analysis, and Characterization

When retrieving an atmospheric profile of interest from sounding measurements, an error analysis and characterization of the retrieved profile is as important as a proper estimate of the profile itself, since the former provides quantitative measures on quality properties of retrieved profiles such as accuracy and resolution and thus indicates their utility for potential applications. Profile retrieval without such estimates is of limited value only. The Bayesian optimal estimation framework rigorously provides estimates of this type in addition to a best estimate of the profile itself and furnishes instructive insights into the mechanisms of the retrieval process.

Applying this framework following *Rodgers* [1976, 1990, 2000], a priori data $\mathbf{x}_{ap}$ on a state $\mathbf{x}$ to be estimated are fused with measurement data $\mathbf{y}$ in a way to obtain a joint estimate $\hat{\mathbf{x}}$ of the state making optimal use of the information provided by $\mathbf{y}$ and $\mathbf{x}_{ap}$, given their uncertainties $\mathbf{S}_\varepsilon$ and $\mathbf{S}_{ap}$. In our context the state $\mathbf{x}$ is either of the desired atmospheric profiles, bending angle profile $\mathbf{x}_\alpha$, refractivity profile $\mathbf{x}_N$, pressure profile $\mathbf{x}_p$, or temperature profile $\mathbf{x}_T$, respectively, the measurement $\mathbf{y}$ corresponds to the excess phase profile $\mathbf{l}$. Regarding error specifications $\mathbf{S}_\varepsilon$ and $\mathbf{S}_{ap}$, the formulation we adopt assumes that all errors involved are unbiased and obey Gaussian statistics, which is reasonably applicable for the case of interest here. Note that by ansatz this does not allow analysis of biases, however, a matter which will be addressed within a complementary ensemble-based empirical error analysis in a forthcoming paper.

The processing steps in the occultation data retrieval chain can be well formulated in a linear way (see section 4; only the step from $\mathbf{x}_N$ to $\mathbf{x}_T$ needs linearization), that is, by constant forward operator matrices $\mathbf{K}$, so that the forward model reads,

$$\mathbf{y} = \mathbf{K}_r \cdot \mathbf{x}_r + \varepsilon \,, \tag{1}$$

where the subscript r denotes either of α, N, p, T, (e.g., r = α implies that the state $\mathbf{x}_\alpha$ is mapped by the linear operator $\mathbf{K}_\alpha$ to the measurement space) and ε denotes measurement noise statistically described by covariance matrix $\mathbf{S}_\varepsilon$. Matrix $\mathbf{K}_r$, formulated in section 4 for the four retrieval products

considered, expresses the physical mechanism of how the measurement $\mathbf{y}$ originates from the state $\mathbf{x}_r$ in the atmosphere (rows of $\mathbf{K}_r$ can be seen as "weighting functions" quantifying the sensitivity of measured values to the state $\mathbf{x}_r$). In addition to (1) describing the measurement process, the second ingredient required within the adopted framework is a priori knowledge on $\mathbf{x}_r$ and its uncertainty in the form of $\mathbf{x}_{ap,r}$ and $\mathbf{S}_{ap,r}$, where the subscript r indicates, as above, the four retrieval products of interest. In this study we supply this prior information invoking the CIRA86aQ_UoG model [*Kirchengast et al.*, 1999], an enhanced version of the well known CIRA-86 climatological model [*Fleming et al.*, 1988] (see further details in section 4).

Utilizing the introduced quantities, the optimal estimation solution of the inverse problem can be written as

$$\hat{\mathbf{x}}_r = \mathbf{x}_{ap,r} + (\mathbf{K}_r^T \mathbf{S}_\varepsilon^{-1} \mathbf{K}_r + \mathbf{S}_{ap,r}^{-1})^{-1} \mathbf{K}_r^T \mathbf{S}_\varepsilon^{-1} (\mathbf{y} - \mathbf{K}_r \mathbf{x}_{ap,r}), \quad (2)$$

$$\hat{\mathbf{S}}_r = (\mathbf{K}_r^T \mathbf{S}_\varepsilon^{-1} \mathbf{K}_r + \mathbf{S}_{ap,r}^{-1})^{-1}, \quad (3)$$

where $\hat{\mathbf{x}}_r$ is the (linear unbiased) optimal estimate of profile $\mathbf{x}_r$, $r \in \{\alpha, N, p, T\}$ and $\hat{\mathbf{S}}_r$ is the associated optimal error covariance estimate. This solution is frequently termed maximum a posteriori (MAP) solution as it is theoretically derived based on maximizing the posterior probability density function (pdf) arising from use of Bayes' theorem given a prior pdf $P(\mathbf{x}_r) \propto \exp[-\frac{1}{2}(\mathbf{x}_r - \mathbf{x}_{ap,r})^T \mathbf{S}_{ap,r}^{-1} (\mathbf{x}_r - \mathbf{x}_{ap,r})]$ and a likelihood pdf $P(\mathbf{y}|\mathbf{x}_r) \propto \exp[-\frac{1}{2}(\mathbf{y} - \mathbf{K}_r\mathbf{x}_r) \mathbf{S}_\varepsilon^{-1} (\mathbf{y} - \mathbf{K}_r\mathbf{x}_r)]$, respectively [*Rodgers*, 2000]. A relevant "asymptotic" property of (2) is that since it yields an unbiased state estimate $\hat{\mathbf{x}}_r$, measurements of the a priori state (i.e., $\mathbf{y} = \mathbf{K}_r\mathbf{x}_{ap,r}$) will lead to getting in turn the a priori state retrieved (i.e., $\hat{\mathbf{x}}_r = \mathbf{x}_{ap,r}$). A relevant property of (3) is its independence of any state $\mathbf{x}$, which allows to perform the error analysis in a generic manner solely based on the errors specifications $\mathbf{S}_\varepsilon$, $\mathbf{S}_{ap,r}$ and on the mapping $\mathbf{K}_r$. This is exactly the way we work out the analysis in section 4.

Profile characterization provides further information on the retrievals including on resolution and on the sensitivity of the retrieved state $\hat{\mathbf{x}}_r$ to the true state, the measurements, and the a priori state. As seen from (2), the retrieved state $\hat{\mathbf{x}}_r$ is a combination of the true state $\mathbf{x}_r$ and the a priori state $\mathbf{x}_{ap,r}$, whereby the true state is known indirectly and only approximately, in a form mapped to measurement space and perturbed, i.e., as a noisy measurement profile $\mathbf{y} + \varepsilon$. In order to study the resolution of $\hat{\mathbf{x}}_r$ and its sensitivities, the following diagnostic expressions are useful (see, e.g., *Rodgers* [2000] for details). The so-called averaging kernel matrix $\mathbf{A}$ is defined by

$$\mathbf{A}_r = \frac{d\hat{\mathbf{x}}_r}{d\mathbf{x}_r} \quad (4)$$

and expresses the sensitivity of the retrieved state $\hat{\mathbf{x}}_r$ to the true state $\mathbf{x}_r$. The rows of $\mathbf{A}_r$, the averaging kernel functions, generally peak at the diagonal value, and the width at half maximum of this peak is a measure of the spatial resolution at the height level of the peak. Furthermore, if the sum over an averaging kernel function, sometimes termed its area, is essentially unity, then virtually all information comes from the measurements, and lower values indicate significant information coming also from the a priori data. The so-called contribution matrix $\mathbf{D}$ (alternatively also termed gain matrix $\mathbf{G}$ [*Rodgers*, 2000]) is defined by

$$\mathbf{D}_r = \frac{d\hat{\mathbf{x}}_r}{d\mathbf{y}} \quad (5)$$

and expresses the sensitivity of $\hat{\mathbf{x}}_r$ to the measurement profile $\mathbf{y}$. The columns of $\mathbf{D}_r$, the contribution functions, also generally peak near the diagonal value, and they quantify how a measurement y_i (at height level z_i if measurements and state share the same grid) contributes to $\hat{\mathbf{x}}_r$. Both matrices can be viewed, besides as sensitivities according to (4) and (5), as operators producing the retrieved state by a linear combination of the form

$$\hat{\mathbf{x}}_r = \mathbf{x}_{ap,r} + \mathbf{A}_r (\mathbf{x}_r - \mathbf{x}_{ap,r}) + \mathbf{D}_r \varepsilon . \quad (6)$$

Comparing (2) and (3) with (6) reveals that within the optimal estimation scheme, both $\mathbf{A}_r$ and $\mathbf{D}_r$ can be written as explicit algebraic expressions in the form

$$\mathbf{A}_r = \hat{\mathbf{S}}_r \mathbf{K}_r^T \mathbf{S}_\varepsilon^{-1} \mathbf{K}_r , \quad \mathbf{D}_r = \hat{\mathbf{S}}_r \mathbf{K}_r^T \mathbf{S}_\varepsilon^{-1} \text{ (i.e., } \mathbf{A}_r = \mathbf{D}_r \mathbf{K}_r). \quad (7)$$

In section 4 we evaluate $\mathbf{A}_r$ and $\mathbf{D}_r$ employing (7). The sensitivity of $\hat{\mathbf{x}}_r$ to the a priori state $\mathbf{x}_{ap,r}$ can be stated analogously to (4) and (5) in the form $d\hat{\mathbf{x}}_r / d\mathbf{x}_{ap,r}$, which leads to a matrix $(\mathbf{I} - \mathbf{A}_r)$, identity matrix minus $\mathbf{A}_r$, expressing this sensitivity. As $(\mathbf{I} - \mathbf{A}_r)$ is readily inferred from $\mathbf{A}_r$, we do not separately discuss it in addition to $\mathbf{A}_r$ in section 4.

For indicating the influence of the a priori data on the retrieval we rather utilize another measure, a height profile $\mathbf{q}_r$ expressing the ratio of the retrieval error to the a priori error,

$$\mathbf{q}_r = 100 \times \sqrt{\text{diag}(\hat{\mathbf{S}}_r)} \,/\, \sqrt{\text{diag}(\mathbf{S}_{ap,r})} , \quad (8)$$

where the factor 100 normalizes $\mathbf{q}_r$ to units percent. The height profile $\mathbf{q}_r$ can be regarded to indicate the percentage of the retrieval error stemming from the a priori error. Roughly speaking, if the percentage is <10%, almost all information is provided by the measurements; if it is >50%, the majority of information comes from the a priori data. Although ignoring the covariances for convenience, the $\mathbf{q}_r$ profile is instructive in that it roughly indicates, for each retrieval product, at which heights a priori data contribute significant information.

4. Application to GNSS Occultation Data Processing

In applying the error analysis and characterization formalism of section 3 for deriving the properties $\hat{\mathbf{S}}_r$, $\mathbf{A}_r$, $\mathbf{D}_r$, and $\mathbf{q}_r$ for all profiles $\mathbf{x}_r$, $r \in \{\alpha, N, p, T\}$, two representative scenarios of measurement quality were selected: An advanced receiver (AR) scenario, where we adopted an unbiased uncorrelated Gaussian error in the excess phase profile $\mathbf{l}$ with a standard deviation of 2 mm at 10 Hz receiver sampling rate, and a standard receiver (SR) scenario, where we changed the standard deviation to 5 mm, respectively. The AR scenario reflects a data quality possible with modern receivers such as the European GNSS Receiver for Atmospheric Sounding (GRAS), foreseen to be flown on the future series of polar-orbiting meteorological operational satellites METOP (first launch scheduled 2005) [*ESA/EUMETSAT*, 1998], while the SR scenario reflects a quality available from the proof-of-concept mission GPS/MET, which delivered highly valuable data within the 1995 to 1997 time frame [*Ware et al.*, 1996; *Rocken et al.*, 1997]. Putting this error into perspective relative to the signal, the latter amounts to only ~1 mm at

mesopause level (~85 km), increasing via ~20 cm at stratopause level (~50 km) and ~20 m at tropopause level (~15 km) to ~1–2 km at the surface. The low mesospheric SNR of retrieval products $\hat{\mathbf{x}}_r$ as visible in Figure 1 is thus not surprising.

The above error specification for $\mathbf{I}$ determines the measurement error covariance matrix at 10 Hz sampling rate, $\mathbf{S}_{\varepsilon,10Hz}$. The squared standard deviations form the diagonal elements (variances) and the off-diagonal elements (covariances) are zero as the errors are assumed uncorrelated. The variances are assumed the same at all heights; that is, we disregard SNR decreases in the troposphere (occurring mainly due to signal defocusing) as these low heights are of secondary interest in this baseline study. While uncorrelated errors in $\mathbf{I}$ are a reasonable approximation, it requires further investigation to what extend correlations might be introduced by clock errors, which may be dominated by correlated flicker-frequency noise due to an underlying random walk or first-order autoregressive process.

We performed the entire analysis on a fixed height-level grid spanning 0 to 120 km, which roughly reflects the Fresnel diffraction limited resolution of the method (increasing with decreasing height; see section 2) and typical smoothing imposed (increasingly more smoothing at greater heights for better noise suppression [e.g., *Steiner et al.*, 1999]). The grid was adopted to be spaced 0.5 km within 0 to 20 km, 2 km within 70 to 120 km, and with spacing linearly increasing from 0.5 to 2 km within 20 to 70 km (slightly adjusted above 60 km to smoothly approach the 70-km level), respectively. While the range of practical interest is below the stratopause, the grid extend up to 120 km is required for methodological reasons, most notably for accurate evaluation of Abelian and hydrostatic integrations [e.g., *Syndergaard*, 1999; *Steiner et al.*, 1999]. This retrieval grid leads to vectors and matrices with dimensions of ~100, which can be processed very efficiently and robustly within the baselined optimal estimation framework.

4.1. Formulation of Input Quantities for the Optimal Estimation Analysis

All required ingredients, $\mathbf{S}_\varepsilon$, $\mathbf{x}_{ap,r}$, $\mathbf{S}_{ap,r}$, and $\mathbf{K}_r$, are formulated on the fixed retrieval grid. Their formulation is described in this section as a prerequisite to discussing the analysis results for each profile $\mathbf{x}_r$, $r \in \{\alpha, N, p, T\}$, in sections 4.2 – 4.6.

The phase measurement error covariance matrix $\mathbf{S}_\varepsilon$ was deduced from $\mathbf{S}_{\varepsilon,10Hz}$ introduced above in two steps: First, the 0.1-s time grid of $\mathbf{S}_{\varepsilon,10Hz}$, t_i, was converted to a height grid, z_i, via the "ray perigee velocity" formula [e.g., *Melbourne et al.*, 1994]

$$z_i = z(t_i) = z_0 - \frac{v_0 \cdot t_i}{1 - D_{LEO} \dfrac{d\alpha[\hat{z}(t_i)]}{dz}}, \qquad (9)$$

where $z_0 = z(t_0=0)$ is the height of occultation start (set to 120 km), v_0 is the "sinking velocity" of the ray purely by geometry (set to 2.5 km s^{-1}), D_{LEO} is the ray perigee distance from receiver (set to 3200 km), and $d\alpha/dz$ is the vertical bending angle derivative (computed using profile $\mathbf{x}_{ap,\alpha}$ described below) with $\hat{z}(t_i \mid i > 1) = z_{i-1} - (z_{i-2} - z_{i-1})$; $\hat{z}(t_1) = z_0 - v_0 t_1$ estimated by invoking previous levels. Second, for each height level of $\mathbf{S}_\varepsilon$, all variance values in $\mathbf{S}_{\varepsilon,10Hz}$ falling into the corresponding height layer were averaged, and the result was divided by the number of values in order to account for the suppression of statistical noise by the averaging (care was taken of fractions of samples crossing layer bounds). The resulting phase error profile is illustrated in Figure 2a for both the AR and the SR scenarios. Since the conversion to the retrieval grid corresponds to significant smoothing (the original 10 Hz rate corresponds to a rather dense height sampling of ~200 m), the phase noise is found suppressed to ~1 mm/~2 mm (AR/SR scenario) at this grid. Given the height-varying spacing of the grid and the nonlinearity of (9) the variance is also no longer constant in $\mathbf{S}_\varepsilon$.

The a priori profiles $\mathbf{x}_{ap,r}$ and a priori error covariance matrices $\mathbf{S}_{ap,r}$ ($r \in \{\alpha, N, p, T\}$) were formulated based on representative $\mathbf{T}$ and $\mathbf{p}$ profiles extracted from the CIRA86aQ_UoG atmosphere climatology model [*Kirchengast et al.*, 1999] and on typical uncertainty estimates, respectively. The March, 40°N, profiles were used, the values of which are identical to the original CIRA-86 tabular model [*Fleming et al.*, 1988] at the tabulated locations; $\mathbf{x}_{ap,T} = \mathbf{T}$ and $\mathbf{x}_{ap,p} = \mathbf{p}$ were directly used as extracted at the retrieval grid from CIRA86aQ_UoG. $\mathbf{x}_{ap,N}$ and $\mathbf{x}_{ap,\alpha}$ were obtained subsequently via $\mathbf{K}_{p:N} \cdot \mathbf{x}_{ap,p}$ and $\mathbf{K}_{N:\alpha} \cdot \mathbf{x}_{ap,N}$, respectively, where the operators $\mathbf{K}_{r:r'}$ transform profile $\mathbf{x}_{ap,r}$ to profile $\mathbf{x}_{ap,r'}$ (these are described in more detail below). Regarding matrices $\mathbf{S}_{ap,r}$, these were prescribed in form of squared RMS uncertainties, $\sigma^2_{ap,i}$, for the diagonal (variance) values, complemented by off-diagonal (covariance) values of the form $\sigma^2_{ap,ij} = \sigma_{ap,i}\, \sigma_{ap,j}\, \exp[-(z_i - z_j)^2/(2L_\sigma^2)]$, which represent Gaussian drop-off correlation with correlation length L_σ. $L_\sigma = 3$ km was used for all matrices $\mathbf{S}_{ap,r}$, reflecting that the background profiles are generally smooth and void of significant variability at scales much smaller than a scale height. However, for highlighting the role of background correlations in the retrieval process, we illustrate below also correlation function results for $L_\sigma = 0.5$ km (with all other settings identical). The RMS uncertainty profiles σ_{ap} were modeled as follows. For $\mathbf{x}_{ap,T}$ an uncertainty of 2 K was assumed from 0 to 20 km, and a linear uncertainty increase from 2 K to 22 K within 20 to 120 km. The uncertainties of the other profiles were specified in relative terms (i.e., as $100 \times \sigma_{ap}/\mathbf{x}_{ap}$ [%]), all in form of linearly increasing uncertainty from 0 to 120 km: For $\mathbf{x}_{ap,p}$ and $\mathbf{x}_{ap,N}$ the uncertainty was assumed to increase from 2% to 18% in this range, while for $\mathbf{x}_{ap,\alpha}$ it was assumed to increase from 4% to 22%.

Figures 2b – 2e illustrate all a priori uncertainties together with the corresponding a priori profile $\mathbf{x}_{ap,r}$; for temperature the uncertainty is depicted for better visualization as interval about the mean profile $\mathbf{x}_{ap,T}$. These "experience-based/educated guess" uncertainties roughly reflect atmospheric model forecast uncertainties (6 to 12 hour forecasts) at troposphere/stratosphere heights and climatological model (e.g., CIRA-86 model) uncertainties at mesospheric heights. In the uncertainties on $\mathbf{x}_{ap,p}$, $\mathbf{x}_{ap,N}$, and $\mathbf{x}_{ap,\alpha}$ also some room is given for forward modeling errors [e.g., *Palmer et al.*, 2000; *Rodgers*, 2000], which increase the more indirect the dependence on the fundamental profile $\mathbf{x}_{ap,T}$ is. Sensitivity tests showed that enlarging/reducing the a priori

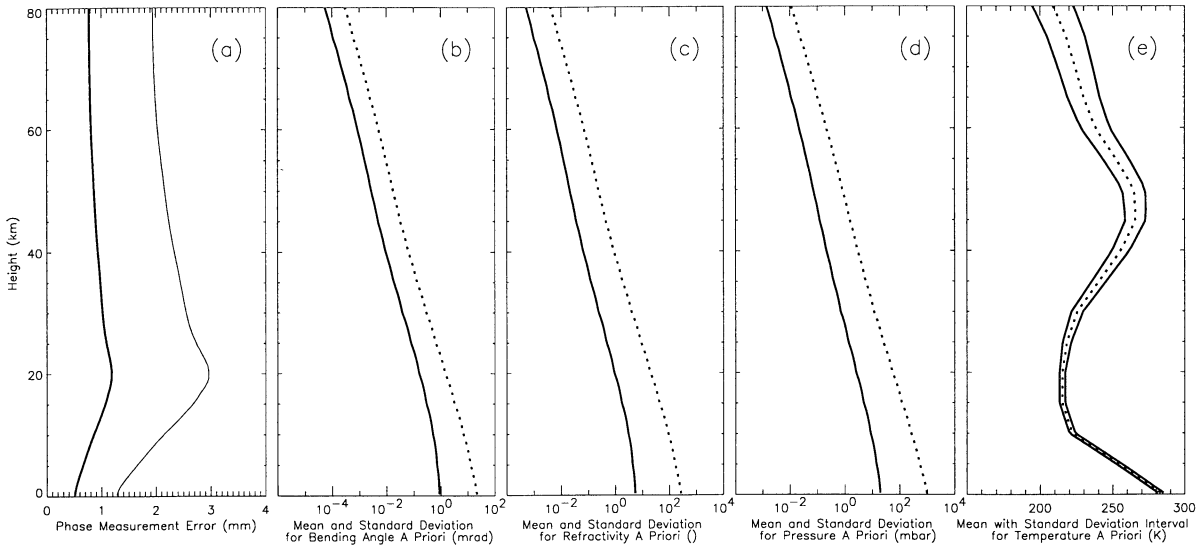

Figure 2. Illustration of inputs to the optimal estimation analysis. (a) Square root of diagonal of the measurement error covariance matrix $\mathbf{S}_\varepsilon$ for the AR (heavy line) and SR (light line) scenario, respectively. (b–e) A priori profiles $\mathbf{x}_{ap,r}$ (dotted) and square root of diagonal of a priori error covariance matrices $\mathbf{S}_{ap,r}$ (solid) for (b) bending angle, (c) refractivity, (d) pressure, and (e) temperature (error depicted as interval about a priori profile).

uncertainties within reasonable limits moderately increases/decreases retrieval errors at high altitudes as well as raises/lowers the height level above which a priori errors dominate. The effect on correlation functions, averaging kernels, and contribution functions is fairly small. These test findings confirm that the scenario results shown below are rather representative.

The forward operators $\mathbf{K}_r$, expressing the dependence of the measured excess phase profile $\mathbf{l}$ on the desired profile $\mathbf{x}_r$, are implemented by exploiting the knowledge that all profiles involved are associated with each other in a chain-like manner by well established physical relations [e.g., *Kursinski et al.*, 1997]. These relations can be utilized to explicitly formulate operators $\mathbf{K}_r$ in matrix form as products of linear sub operators $\mathbf{K}_{r:r'}$, where the latter perform a specific forward modeling step, from profile $\mathbf{x}_r$ to profile $\mathbf{x}_{r'}$, within the chain to profile $\mathbf{l}$. For r, r' $\in \{\alpha, N, p, T\}$ the operators $\mathbf{K}_r$ read

$$\begin{aligned} \mathbf{K}_\alpha &= \mathbf{K}_{\alpha:l},\ \mathbf{K}_N = \mathbf{K}_\alpha \cdot \mathbf{K}_{N:\alpha}, \\ \mathbf{K}_p &= \mathbf{K}_N \cdot \mathbf{K}_{p:N},\ \mathbf{K}_T = \mathbf{K}_N \cdot \mathbf{K}_{T:N}, \end{aligned} \tag{10}$$

which involves in total four suboperators $\mathbf{K}_{r:r'}$ in the chains. For this study we utilize in $\mathbf{K}_{\alpha:l}$ the sinking velocity of the ray impact height to map α to excess Doppler d and Doppler integration to map d to excess phase l, in $\mathbf{K}_{N:\alpha}$ the forward Abel transform to map N to α, in $\mathbf{K}_{p:N}$ the hydrostatic equation to map p to N, and in $\mathbf{K}_{T:N}$ the equation of state and the hydrostatic integral to map (linearized) T to N, respectively. The specific implementation of each of the four suboperators is discussed in the context of sections 4.2 to 4.5.

Ingredients $\mathbf{S}_\varepsilon$, $\mathbf{x}_{ap,r}$, $\mathbf{S}_{ap,r}$, and $\mathbf{K}_r$ can all be prescribed in a different way than here without any change to the error analysis and characterization formalism given by (3) to (8) in section 3. For example, one could use more sophisticated a priori matrices $\mathbf{S}_{ap,r}$ (based on formulations existing in analysis systems operated by meteorological service centers) and/or improved forward operators. For the latter it is also readily possible, if desired, to account for nonlinearities in suboperators $\mathbf{K}_{r:r'}$: In the case when $\mathbf{K}_r(\mathbf{x}_r)$ replaces $\mathbf{K}_r \cdot \mathbf{x}_r$ in (1), the problem is linearized, (2) takes an iterative form while (3) to (8) are unchanged, and $\mathbf{K}_{r:r'}$ becomes a Jacobian of form $\mathbf{K}_{r:r'} = \partial \mathbf{K}_{r:r'}(\mathbf{x}_r)/\partial \mathbf{x}_r$ (see *Rodgers* [2000] for details). Such linearized formulation is, for example, useful if in a moist atmosphere $\mathbf{K}_{T:N}$ is generalized to a nonlinear operator $\mathbf{K}_{(T,q,p0):N}$ jointly mapping temperature, humidity, and surface pressure to refractivity [*Healy and Eyre*, 2000; *Palmer et al., 2000*] (the linearized $\mathbf{K}_{T:N}$ in our dry air case is still an explicit analytical quantity; section 4.5). Despite such potential for enhancements we believe that our relatively simple formulation is well selected for demonstrating the approach and for providing a sensible baseline analysis.

4.2. Analysis and Results for Bending Angle Profiles

The step from excess phase profile $\mathbf{l}$ to bending angle profile $\mathbf{x}_\alpha$, the first step in the retrieval chain according to (10), is usually performed sample by sample by first computing the time derivative of excess phase l to obtain excess Doppler d and then using precise knowledge of positions and velocities of transmitter and receiver satellites (obtained from precise orbit determination, POD) and Snell's law under spherical symmetry to compute bending angle α as a function of impact parameter a [e.g., *Kursinski et al.*, 1997]. This can be implemented in different slightly varying ways [e.g., *Fjeldbo et al.*, 1971; *Vorob'ev and Krasil'nikova*, 1994; *Melbourne et al.*, 1994; *Hoeg et al.*, 1995; *Gorbunov et al.*, 1996] either in an iterative or in a linearized form. Furthermore, the resulting profile $\alpha_i(a_i)$ is generally improved and smoothed at high altitudes by merging it with a model profile $\alpha_{mod,i}(a_i)$ (statistical optimization; see sections 1 and 2).

For this study we do not need the inverse but rather the forward process, which is generally easier to formulate as it follows the "cause-to-effect" direction, i.e., is aligned with how the physical mechanisms work. In formulating the required mapping (see Equations (10)),

$$\mathbf{l} = \mathbf{K}_\alpha \cdot \mathbf{x}_\alpha = \mathbf{K}_{\alpha:\mathrm{l}} \cdot \mathbf{x}_\alpha \,, \tag{11}$$

we exploit that the relation of α and d is well approximated, for the purpose of error analysis and characterization on which we focus here, by the linear form [*Syndergaard*, 1999]

$$d(t) = -\frac{da}{dt}\alpha(a) \,, \tag{12}$$

expressing that the time derivative of a, in other words the sinking velocity of the ray impact height (a with Earth's radius R_E subtracted), maps α to d. Note that for estimation of the mean rather than of covariance and characterization properties, i.e., when utilizing (2), da/dt in (12) should be replaced by v_0, the sinking velocity of the ray purely by geometry (see Equation (9)) [*Melbourne et al.*, 1994; *Syndergaard*, 1999].

In order to apply (12) to our fixed-height retrieval grid, $t_i(z_i)$ and $a_i(z_i)$ are needed. We utilized a rearranged Equation (9) to obtain $t_i(z_i)$ and invoked profile $\mathbf{x}_{ap,N}$ to obtain $a_i(z_i) = (R_E + z_i)(1+10^{-6}N(z_i))$, where R_E was set to 6371.0 km. Finally, in order to map $d(t)$ to l, a simple time integration over $d(t)$ from t_0 to $t_i(z_i)$ was applied, which yields $l_i(z_i)$. Regarding practical implementation of $\mathbf{K}_{\alpha:\mathrm{l}}$, a standard three-point finite difference scheme was used for da/dt and a standard trapezoidal rule for the integration over $d(t)$, respectively (both for varying grid spacing).

Inserting $\mathbf{K}_\alpha$ together with $\mathbf{S}_\varepsilon$ and $\mathbf{S}_{ap,\alpha}$ formulated in section 4.1 into (3), (7), and (8), we computed covariance matrix $\hat{\mathbf{S}}_\alpha$, characterization matrices $\mathbf{A}_\alpha$ and $\mathbf{D}_\alpha$, and vector $\mathbf{q}_\alpha$, respectively. For both the AR and SR scenarios, Figure 3 illustrates these quantities in terms of absolute and relative RMS error profiles (diagonal $\sqrt{\mathbf{S}_{\alpha,ii}}$ and 100 x $\sqrt{\mathbf{S}_{\alpha,ii}}/\hat{\mathbf{x}}_{\alpha,i}$) and mean profile ($\hat{\mathbf{x}}_\alpha = \mathbf{x}_{ap,\alpha}$) (Figure 3a), selected correlation functions (rows $\mathbf{S}_{\alpha,ij}/\sqrt{\mathbf{S}_{\alpha,ii} \cdot \mathbf{S}_{\alpha,jj}}$) (Figures 3b, 3c; correlation length L_σ = 0.5 km for Figure 3c), selected averaging kernel functions (rows $\mathbf{A}_{\alpha,ij}$) (Figure 3d), selected contribution functions (columns $\mathbf{D}_{\alpha,ij}$) (Figure 3e), and retrieval-to-a priori error ratio profiles ($\mathbf{q}_\alpha$) (Figure 3f).

The RMS error profiles (Figure 3a) indicate the magnitude of bending angle errors, which are found to be smaller than 1% below ~43 km/~37 km in the AR/SR scenario (dotted horizontal lines) and at absolute values of ~0.6 μrad/1.4 μrad. These error levels are consistent with what the two scenarios intend to reflect [*ESA/EUMETSAT*, 1998; *Rocken et al.*, 1997] and confirm their utility as advanced and standard sensor baselines. The errors below 10 km, though showing a not unreasonable increase, should be interpreted with caution as the present formulation disregards major error sources due to significantly enhanced vertical and horizontal variability in atmospheric parameters (especially moisture) in the troposphere [e.g., *Gorbunov et al.*, 1996; *Gorbunov and Gurvich*, 1998].

The correlation functions, averaging kernel functions, and contribution functions (Figures 3b to 3e) are rather independent of scenario from the stratopause downward, since the a priori uncertainty exerts rather small influence there (Figure 3f) and because $\mathbf{S}_\varepsilon$ differs between the two scenarios from our definition of $\mathbf{S}_{\varepsilon,10Hz}$ only by a scalar constant (factor 2.5). Thus only the AR scenario results are displayed in Figures 3b to 3e. This finding, directly from inspecting (3) and (7), implies that the overall magnitude of measurement errors only marginally affects the correlation structure and the sensitivity quantities below the stratopause. This applies to subsequent retrieval products as well.

On the other hand, comparing Figure 3b (L_σ = 3 km) with Figure 3c (L_σ = 0.5 km) indicates the significance of the correlation structure of the a priori errors for the correlation structure of the retrieval errors. The L_σ = 0.5 km case is instructive in that it nicely reflects the differential relation of l and d via the anticorrelation of errors at adjacent levels (below the stratopause, where the level spacing is sufficiently small). At least at heights above ~30 km, where it is always advisable to fuse in a priori data, this is of minor practical relevance, however, since retrieval algorithms usually use rather smooth a priori profiles with a correlation structure more reasonably reflected by the baseline case with L_σ = 3 km (e.g., from the CIRA [*Fleming et al.*, 1988; *Kirchengast et al.*, 1999] or MSIS [*Hedin*, 1991] models). As a general rule, the correlation narrows with decreasing height along with the decreasing magnitude of the sinking velocity da/dt in $\mathbf{K}_{\alpha:\mathrm{l}}$ and the decreasing a priori influence, respectively. The L_σ = 3 km result is similar to the corresponding bending angle correlation results of *Syndergaard* [1999], though the major cause of correlation spread in the latter work was excess phase filtering (i.e., a different mapping operator) rather than a priori correlations. This indicates the important dependence of error correlations on the specific implementation of operators $\mathbf{K}_{r:r'}$ (or $\mathbf{K}^{-1}_{r:r'}$ in case of a classical inversion chain such as used in the latter work). In other words, though the scenario results worked out here are representative and give a good baseline idea, a specific error analysis should be performed for each specific processing setup. The generic framework proposed here is one excellent candidate for this purpose; a complementary one is ensemble-based empirical error analysis which will be dealt with in a forthcoming paper.

The averaging kernel functions (Figure 3d) indicate, within the formulation used, a resolution for $\hat{\mathbf{x}}_\alpha$ of ~4 km at stratopause heights and of ~2 km at tropopause heights, respectively. The magnitude of the peaks found below unity (~0.3 to 0.5) indicates a moderate oversampling (i.e., more samples than independent pieces of information in the retrieved profile). This is expected in our case where the measurement grid of profile $\mathbf{l}$ is for convenience identical to the retrieval grid. Thus any mapping involving neighborhood values (such as differentiation) somewhat blurs the resolution. More optimized setups would sample the measurements roughly at twice the vertical Fresnel zone diameter (see Section 2), which would allow somewhat improved resolution but with somewhat degraded accuracy, given an otherwise identical processing setup. For example, if the resolution were optimized toward 1 km for the AR scenario, the errors $\sqrt{\mathbf{S}_{\alpha,ii}}$ would in turn go up toward 1 μrad.

The contribution (or gain) functions (Figure 3e) show that because of the differential relation between $\mathbf{l}$ and $\hat{\mathbf{x}}_\alpha$, a phase measurement at any given level contributes most to $\hat{\mathbf{x}}_\alpha$ right

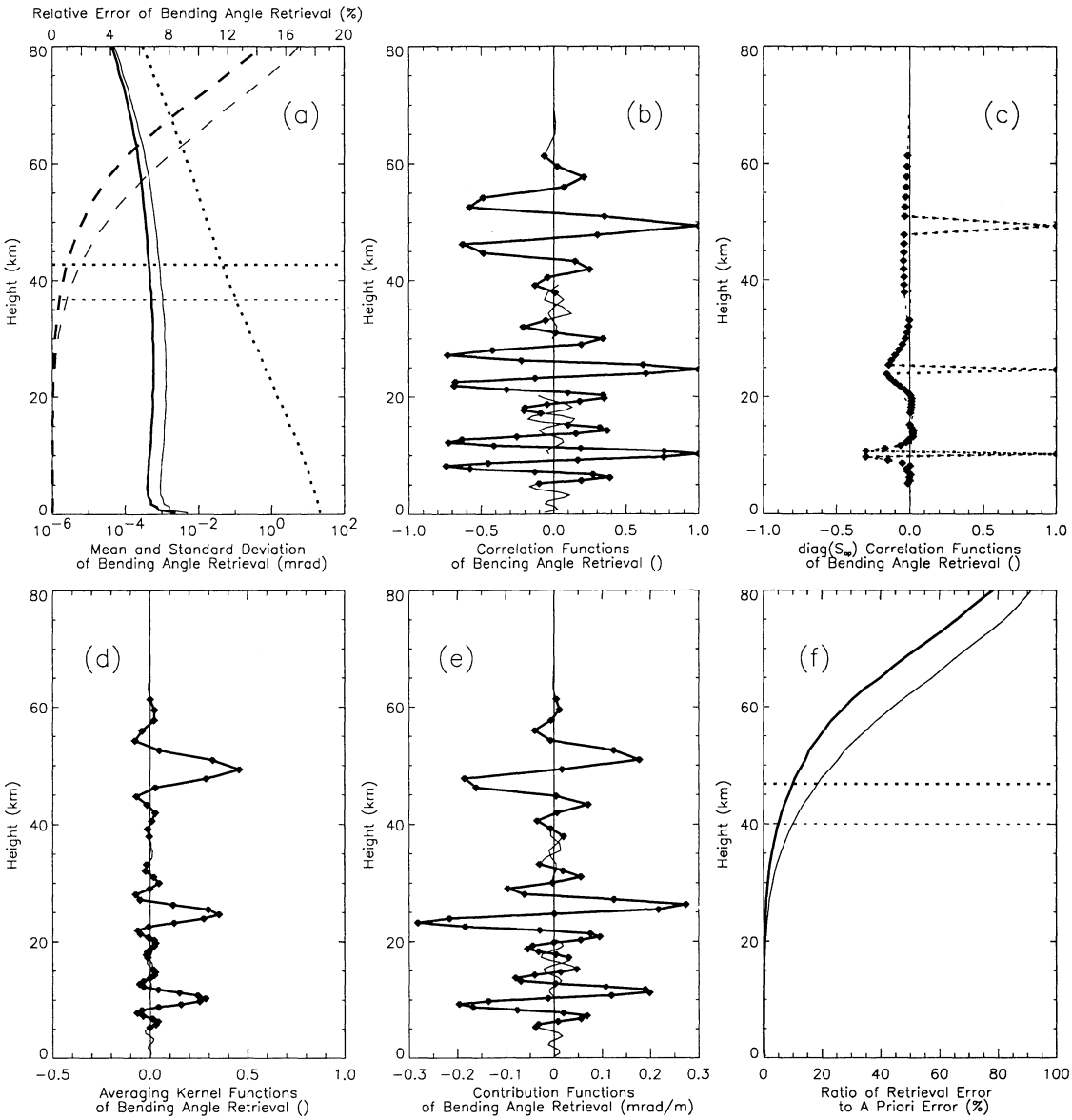

Figure 3. Bending angle retrieval results for AR scenario (heavy lines) and SR scenario (light lines, Figures 3a and 3f) given L_σ = 3 km (except Figure 3c, L_σ = 0.5 km). (a) Absolute (solid) and relative (dashed) unbiased RMS error; mean (=a priori) profile (dotted); 1% accuracy heights (dotted horizontal). (b) L_σ = 3 km and (c) L_σ = 0.5 km (hinted by "diag(S_{ap})") correlation functions for three representative heights (levels ~10 km, ~25 km, ~50 km; ranges ~10±10 km, ~25±15 km, ~50±20 km; retrieval grid levels: small diamond symbols within heavy-line "core region" of functions). (d) Averaging kernel functions and (e) contribution functions for three representative heights (same format as Figures 3b and 3c). (f) Retrieval-to-a priori error ratio; heights where ratio is 10% (dotted horizontal).

above and below. The magnitude of the peaks of ~0.2–0.25 μrad mm^{-1} indicates that a change (or error) of 2 mm in phase at some level will contribute ~0.5 μrad bending angle change (or error) between adjacent levels above and below. This magnitude is consistent with the absolute RMS error of ~0.6 μrad seen in Figure 3a for the AR scenario.

The retrieval-to-a priori error ratio profiles (Figure 3f) instructively illustrate that almost all information in $\hat{\mathbf{x}}_\alpha$ is coming from the measurements ($\mathbf{q}_{\alpha,i} < 10\%$) at heights below ~47 km/~40 km for the AR/SR scenario (dotted horizontal lines), while a priori information starts to dominate ($\mathbf{q}_{\alpha,i} >$ 50%) in the mesosphere for both scenarios. Note, though, that the influence of the a priori correlation spread reaches significantly further down than the "variance-only" quantity $\mathbf{q}_\alpha$ signifies, especially since $\mathbf{S}_\varepsilon$ contains no correlation so that $\hat{\mathbf{S}}_r$ (Equation (3)) still "feels" the covariance function wings in $\mathbf{S}_{ap,r}$ even when its variances are already small. Figure 3f also indicates the excellent capability of (2) to intrinsically perform statistical optimization in a rigorous manner in the sense of unbiased optimal fusion of the measurements with a priori knowledge ($\mathbf{x}_{ap,\alpha}$, $\mathbf{S}_{ap,\alpha}$); an aspect worth noting given the prominent role played by statistical optimization of

bending angle profiles, in one or another approximation, in most current retrieval algorithms (see section 2). Moreover, other than the usual fusion of bending angle data and model at retrieval product level, (2) requires specification of data covariances at the more raw measurement level only ($\mathbf{S}_\varepsilon$), where it is more simple to quantify.

4.3. Analysis and Results for Refractivity (and Density) Profiles

The processing of excess phase profile $\mathbf{l}$ to refractivity profile $\mathbf{x}_N$ requires a forward operation from refractivity to bending angle, $\mathbf{K}_{N:\alpha}$, in addition to mapping $\mathbf{K}_{\alpha:l}$ used from $\mathbf{x}_\alpha$ to $\mathbf{l}$ (Equation (11)). The complete mapping reads (see Equations (10))

$$\mathbf{l} = \mathbf{K}_N \cdot \mathbf{x}_N = \mathbf{K}_{\alpha:l} \cdot \mathbf{K}_{N:\alpha} \cdot \mathbf{x}_N \cdot \qquad (13)$$

In formulating $\mathbf{K}_{N:\alpha}$, we exploit the classical integral relation of bending angle α and refractivity N, a forward Abel transform [e.g., *Fjeldbo et al.*, 1971; *Kursinski et al.*, 1997] valid under the reasonable assumption of spherical symmetry of the atmosphere over a few hundred kilometers near occultation ray perigee locations. The Abel transform (or its inverse counterpart) is used to implement $\mathbf{K}_{N:\alpha}$ (or $\mathbf{K}^{-1}_{N:\alpha}$), in one way or another, in all current retrieval algorithms that we are aware of, because it can be expanded upon only by additional prior information on horizontal variability. Using the convenient approximation $10^{-6} dN(a)/da \cong d\ln n(a)/da$ (refractive index $n = 1 + 10^{-6}N$), we write the transform as

$$\alpha_i(a_i) = -2\times10^{-6} a_i \int_{a=a_i}^{\infty} \frac{dN(a)}{da} \frac{da}{\sqrt{(a^2 - a_i^2)}} , \qquad (14)$$

where the integration over the refractivity gradient profile $dN(a)/da$ theoretically runs over the full upward half-space above the height level of interest $z_i(a_i)$; practically, we can comfortably use 120 km as upper integral bound [*Hocke et al.*, 1997]. In order to utilize (14) on the fixed-height grid, again $a_i(z_i) = (R_E + z_i)\ (1+10^{-6}N(z_i))$ is invoked (see section 4.2). The actual implementation of $\mathbf{K}_{N:\alpha}$ invoked a matrix formulation of (14) by *Steiner et al.* [1999]. A three-point finite difference scheme of type $y_i(\ln y_{i+1} - \ln y_{i-1})/(2dx)$ (for varying grid spacing) was used to represent $dN(a)/da$ and the matrix operator "$\overline{\overline{A}}$" of *Steiner et al.* [1999] (times the factor $2\times10^{-6}a_i$) to represent the integration, respectively. Left-multiplying $\mathbf{K}_{N:\alpha}$ by $\mathbf{K}_{\alpha:l}$ according to (13) then yields the complete mapping $\mathbf{K}_N$.

Inserting $\mathbf{K}_N$ together with $\mathbf{S}_\varepsilon$ and $\mathbf{S}_{ap,N}$ formulated in section 4.1 into (3), (7), and (8), we computed covariance matrix $\hat{\mathbf{S}}_N$, characterization matrices $\mathbf{A}_N$ and $\mathbf{D}_N$, and vector $\mathbf{q}_N$, respectively. For both the AR and SR scenarios, Figure 4 illustrates these quantities for the refractivity retrieval in the same format as Figure 3 did for the bending angle retrieval.

The RMS error profiles (Figure 4a) are found to be smaller than 1% below ~49 km/~43 km in the AR/SR scenario (dotted horizontal lines) and at absolute values of about 0.003/0.007 (N units). This (unbiased) error level is consistent with previous findings, as was noted above for bending angles, which is to be expected as operation $\mathbf{K}_{N:\alpha}$ (or $\mathbf{K}^{-1}_{N:\alpha}$) generally utilizes an Abel transform. The tropospheric error estimates, and also to some extent the lower stratospheric ones, are certainly overly optimistic, however, since we disregarded tropospheric complexities, especially the "forward modeling errors" due to the assumption of spherical symmetry, which simply means ignoring horizontal variability [e.g., *Eyre*, 1994; *Kursinski et al.*, 1997; *Ahmad and Tyler*, 1999; *Palmer et al.*, 2000].

Comparing the correlation functions of Figure 4b (L_σ = 3 km) and Figure 4c (L_σ = 0.5 km) shows the important role of the correlation structure of the a priori errors also for the refractivity retrieval: The L_σ = 0.5 km case (Figure 4c) maintains the small correlation spread seen for the bending angle error correlation (Figure 3c) and the L_σ = 3 km case again shows the dominance of the a priori error correlation structure (the change in correlation structure between Figures 3b and 4b is relatively small, the negative correlation peaks are slightly reduced). This finding indicates that in order to keep correlation structure simple and spread small, it is advisable to fuse in a priori data only down to heights where they indeed benefit the processing (>30 km is sufficient from our experience).

The averaging kernel functions (Figure 4d) exhibit no appreciable change from Figure 3d, i.e., adding $\mathbf{K}_{N:\alpha}$ does not significantly affect the resolution. Because of $\mathbf{K}_{N:\alpha}$, the contribution functions (Figure 4e) undergo a small change (see Figures 3e and 4e) somewhat akin to the correlation structure change (see Figures 3b and 4b); regarding the relation between $\mathbf{l}$ and $\hat{\mathbf{x}}_N$, a phase measurement at any given level contributes most to $\hat{\mathbf{x}}_N$ at this level plus slightly above and leads to some compensatory (negative) contribution especially over a few levels below. This is consistent with the results of the impulse response approach of *Kursinski et al.* [1997] (note at this point that the columns of $\mathbf{A}_r$, in fact, contain the impulse responses of $\hat{\mathbf{x}}_r$ to unit perturbations in values $\mathbf{x}_{r,i}$ [*Rodgers*, 2000]). The magnitude of the dominating positive peaks of ~1.5 N units m^{-1} (or 0.0015 mm^{-1}) indicate that a change (or error) of 2 mm in phase at some level will contribute ~0.003 N units refractivity change (or error) at this level. This magnitude is perfectly consistent with the absolute RMS error of ~0.003 N units seen in Figure 4a for the AR scenario. The retrieval-to-a priori error ratio profiles (Figure 4f) exhibit no significant change from Figure 3f, i.e., performing the optimal estimation at refractivity rather than bending angle level does not affect the overall manner in which a priori information contributes to the state estimate $\hat{\mathbf{x}}_r$.

The refractivity results apply to density as well. As mass density ρ is proportional to refractivity N in dry air via the constant factor $k_{N:\rho} = \overline{M}/(c_1 R) = 4.489\times10^{-3}$ kg m^{-3} ($\overline{M}$ = 28.964 kg kmol^{-1} is the mean molar mass of air, c_1 = 77.60 K mbar^{-1} is the dry air refractivity constant, and R = 8314.5 J K^{-1} kmol^{-1} is the universal gas constant), the results shown for N are readily rescaled to ρ by observing that $\mathbf{x}_{ap,\rho} = k_{N:\rho} \cdot \mathbf{x}_{ap,N}$, $\mathbf{S}_{ap,\rho} = k^2_{N:\rho} \cdot \mathbf{S}_{ap,N}$, and $\mathbf{K}_{\rho:\alpha} = \mathbf{K}_{N:\alpha} / k_{N:\rho}$, respectively. This simply implies, as seen via (3), (7), and (8), that the absolute RMS error profiles and the contribution functions for ρ are $k_{N:\rho}$ times the ones for N, while the relative errors, the correlation functions, the averaging kernel functions, and the retrieval-to-a priori error ratio profile remain the same.

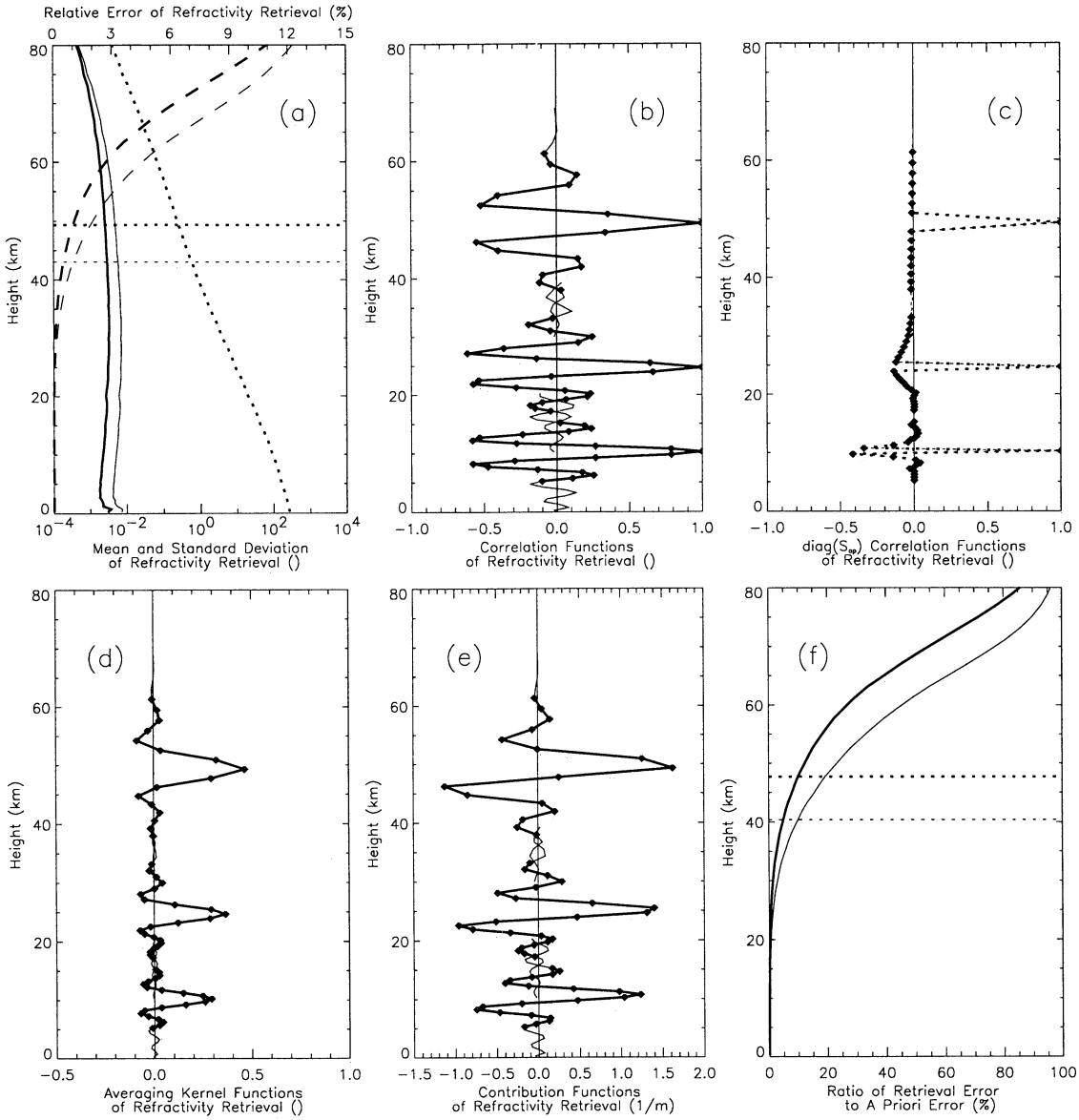

Figure 4. Refractivity retrieval results for AR scenario (heavy lines) and SR scenario (light lines, Figures 4a and 4f) given L_σ = 3 km (except Figure 4c, L_σ = 0.5 km). Same format as Figure 3; see Figure 3 caption for description.

4.4. Analysis and Results for Pressure Profiles

The conversion of excess phase profile **l** to pressure profile $\mathbf{x}_p$ requires, in addition to mapping $\mathbf{K}_N$ used from $\mathbf{x}_N$ to **l** (Equation (13)), a further forward operation from pressure to refractivity, $\mathbf{K}_{p:N}$. The full mapping reads (see Equations (10))

$$\mathbf{l} = \mathbf{K}_p \cdot \mathbf{x}_p = \mathbf{K}_{\alpha:l} \cdot \mathbf{K}_{N:\alpha} \cdot \mathbf{K}_{p:N} \cdot \mathbf{x}_p \,. \tag{15}$$

We use the hydrostatic law in differential form to formulate $\mathbf{K}_{p:N}$, which is the standard relation for this operation as the atmosphere is very close to hydrostatic equilibrium [e.g., *Salby*, 1996] (more precisely, classical inversion chains requiring $\mathbf{K}_{p:N}^{-1}$ use the law in integral form; e.g., *Kursinski et al.* [1997]). It reads for our purpose

$$\frac{1}{\rho(z)}\frac{dp(z)}{dz} = -g(z) \;\Leftrightarrow$$
$$N(z) = -\frac{1}{k_{N:\rho}\, g(z)}\frac{dp(z)}{dz}, \tag{16}$$

where the dry-air proportionality $\rho(z) = k_{N:\rho} \cdot N(z)$, with $k_{N:\rho} = 4.489\times10^{-3}$ kg m^{-3} as defined above, was invoked and where $g(z)$ is the acceleration of gravity, which we utilized in the same latitudinal mean form $g(z) = 9.807$ m s^{-2} $R_E^2/(R_E + z)^2$ as used by *Steiner et al.* [1999]. In implementing $\mathbf{K}_{p:N}$ based on (16), the same type of three-point finite difference scheme was used to represent $dp(z)/dz$ as was used in (14) to represent $dN(a)/da$. Left-multiplying $\mathbf{K}_{p:N}$ by $\mathbf{K}_N = \mathbf{K}_{\alpha:l} \cdot \mathbf{K}_{N:\alpha}$ then yields the complete mapping $\mathbf{K}_p$ (see Equations (13) and (15)).

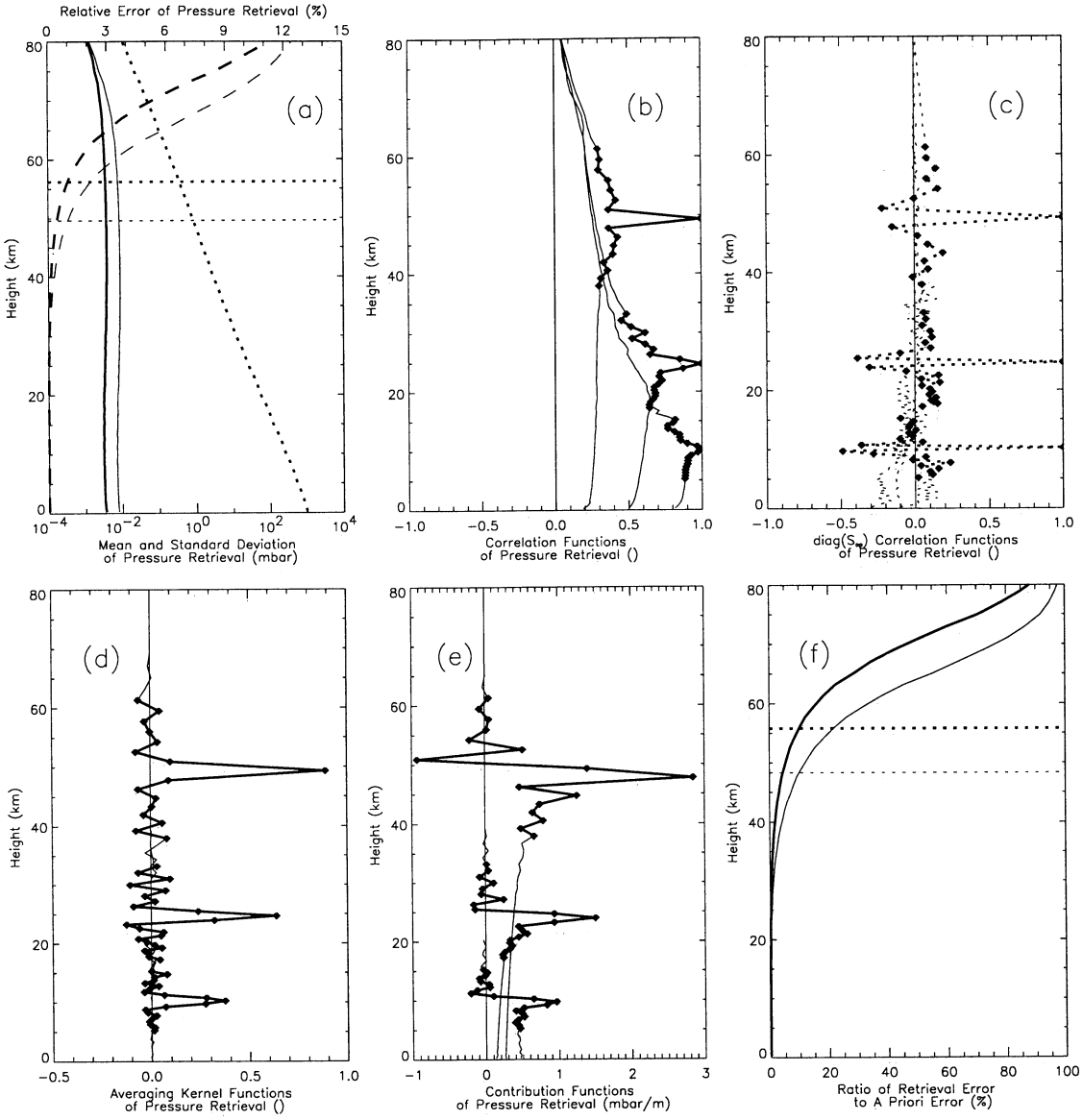

Figure 5. Pressure retrieval results for AR scenario (heavy lines) and SR scenario (light lines, Figures 5a and 5f) given L_σ = 3 km (except Figure 5c, L_σ = 0.5 km). Different from Figure 3, the correlation functions (Figures 5b and 5c) are depicted over the full height range, and the contribution functions (Figure 5e) are depicted down to the surface. Otherwise same format as Figure 3; see Figure 3 caption for description.

Inserting $\mathbf{K}_p$ together with $\mathbf{S}_\varepsilon$ and $\mathbf{S}_{ap,p}$ formulated in section 4.1 into Equations (3), (7), and (8), we computed covariance matrix $\hat{\mathbf{S}}_p$, characterization matrices $\mathbf{A}_p$ and $\mathbf{D}_p$, and vector $\mathbf{q}_p$, respectively. For both the AR and SR scenarios, Figure 5 illustrates these quantities for the pressure retrieval in the same format as used for Figures 3 (bending angle) and 4 (refractivity) above. The RMS error profiles (Figure 5a) are found to be smaller than 1% below ~56 km/~49 km in the AR/SR scenario (dotted horizontal lines) and at absolute values of ~0.004/0.009 mbar. This pressure error magnitude due to (unbiased) phase measurement noise as prescribed is again reasonable down into the lower stratosphere, where it starts to be increasingly too optimistic, since quasi-random forward modeling errors not subsumed into $\mathbf{S}_\varepsilon$ become increasingly dominant as noted from other perspectives already in earlier sections.

A comparison of the correlation functions, Figure 5b (L_σ = 3 km) and Figure 5c (L_σ = 0.5 km), with those of Figure 4 indicates as most characteristic feature the correlation spread introduced by the integral relation of N to p, the degree of which is heavily driven by the a priori error correlation spread in $\mathbf{S}_{ap,p}$ (in Figure 5c, and slightly also in Figure 5b, the "jitter" in correlation function wings appears since operator $\mathbf{K}_p$ (Equation (15)) drives the numerical estimation of $\hat{\mathbf{S}}_p$ (Equation (3)) to gradually approach numerical instability while L_σ approaches zero; except for the jitter, also the results for L_σ = 0.5 km are still robust, however). Furthermore, background correlation levels in $\hat{\mathbf{S}}_p$ are found to significantly

increase with decreasing height in the practically relevant case of some spread in $\mathbf{S}_{ap,p}$ (represented by $L_\sigma = 3$ km, Figure 5b). With classical step-by-step inversion and when involving no a priori information, *Syndergaard* [1999] even found very extreme background correlation estimates for $\mathbf{S}_p$ (mostly >0.99!) though the correlation structure estimate for $\mathbf{S}_N$ was comparable to ours (but with different cause as noted earlier); for tests involving "heuristic statistical optimization" [*Hocke*, 1997; *Steiner et al.*, 1999], reduced background correlation was reported.

A clear understanding of these partly surprising estimates of the structure of $\mathbf{S}_p$ can be gained on the basis of an explicit analytical expression given by *Rieder and Kirchengast* [2001, equation (20)] for the dependence of $\hat{\mathbf{S}}_{p,ij}$ on $\hat{\mathbf{S}}_\rho$ when the discretized hydrostatic integral is used as operator $\mathbf{K}_{p:\rho}^{-1}$. The expression reveals that each covariance element $\hat{\mathbf{S}}_{p,ij}$ is closely proportional (exactly proportional if $g(z)$ and grid spacing $\Delta z(z)$ are assumed constant) to the sum over all elements in the submatrix of $\hat{\mathbf{S}}_\rho$ down to element $\hat{\mathbf{S}}_{\rho,ij}$ (in other words, the sum over the upper partition matrix lower-right bounded by $\hat{\mathbf{S}}_{\rho,ij}$). This implies that the covariance elements $\hat{\mathbf{S}}_{N,(ij|i\neq j)}$ play a crucial role both in suppressing the variances $\hat{\mathbf{S}}_{p,ii}$ compared to a misleadingly pessimistic variance-only sum (by the negative correlation peaks near the main peak) and in significantly blurring the correlation structure in $\hat{\mathbf{S}}_p$ (as a full upper partition of $\hat{\mathbf{S}}_N$ is aggregated in each $\hat{\mathbf{S}}_{p,ij}$), respectively. The extreme correlations found by *Syndergaard* [1999] in absence of a priori constraints resulted since the absolute variances $\hat{\mathbf{S}}_{N,ii}$ were constant rather than decreasing (Figure 5a) above the stratopause in that case, which largely diminishes the otherwise dominating role of elements at and close to the height of interest. Utilization of prior information at high altitudes is thus vital to mitigate correlation spread in pressure and in the subsequent product temperature. The characteristic that the correlation functions depict a sharp drop-off near the peaks and then a slower drop-off over the wings is also a direct effect of the summation: For the diagonal elements $\hat{\mathbf{S}}_{p,ii}$, and to a height-dependent extent also for the adjacent side-diagonal ones, the negative covariances in $\hat{\mathbf{S}}_{N,(ij|i\neq j)}$ can provide only weak compensation for the high values at and very close to the height of interest; for the off-diagonal elements, however, the covariance aggregation does act as an efficient smoother.

The averaging kernel functions (Figure 5d, compare with Figure 4d) indicate that the "sharp drop-off" characteristic introduced by $\mathbf{K}_{p:N}$ not only leads to pronounced peaks in $\hat{\mathbf{S}}_p$ but apparently also leads to somewhat improving the resolution in $\hat{\mathbf{x}}_p$ relative to the one in earlier products. While it sounds surprising at first glance that a subsequent retrieval product should exhibit better resolution than its predecessors, it may happen in indirect measurements that a mapping $\mathbf{K}_r = \mathbf{K}_{r'} \cdot \mathbf{K}_{r:r'}$ performs a somewhat different trade-off between resolution (rows of $\mathbf{A}_r$) and accuracy (rows of $\hat{\mathbf{S}}_r$) than its submapping $\mathbf{K}_{r'}$. Note also, however, that the width of the main peak of the averaging kernel functions is only a rough scalar measure of resolution; inspecting the full functions shows that while the peaks in $\mathbf{A}_p$ are sharper than in $\mathbf{A}_N$, the wings exhibit stronger oscillations.

The contribution functions (Figure 5e) show, as expected after hydrostatic integration, that a phase change at a given level contributes most at this level and adjacent levels but (with decreased strength) also to all levels further below. The magnitude of the dominating positive peaks of ~1–3 mbar m^{-1} (or 0.001–0.003 mbar mm^{-1}) indicates that a change (or error) of 2 mm in phase at some level will contribute ~0.004 mbar pressure change (or error) at this level. This magnitude is again consistent with the absolute RMS error of ~0.004 mbar seen in Figure 5a for the AR scenario. The retrieval-to-a priori error ratio profiles (Figure 5f) indicate that the estimate $\hat{\mathbf{x}}_p$ is associated with more fractional improvement than $\hat{\mathbf{x}}_N$ (both were constrained by the same relative a priori errors; see section 4.1), in line with the effective suppression of RMS errors in $\hat{\mathbf{x}}_p$ by the hydrostatic integration, as addressed above.

4.5. Analysis and Results for Temperature Profiles

The process from excess phase profile $\mathbf{l}$ to temperature profile $\mathbf{x}_T$ can be formulated, for a tangent-linear state $\mathbf{x}_{\delta T}$ of $\mathbf{x}_T$ obtained via a linearization $\mathbf{x}_T = \mathbf{x}_{0,T} + \mathbf{x}_{\delta T}$, in the same way as the process for $\mathbf{x}_p$: A forward operation from (linearized) temperature to refractivity, $\mathbf{K}_{T:N}$, is added to the mapping $\mathbf{K}_N$ used from $\mathbf{x}_N$ to $\mathbf{l}$ (Equation (13). The complete mapping from $\mathbf{x}_{\delta T}$ to a corresponding phase profile change $\delta\mathbf{l}$ reads (see Equations (10))

$$\delta\mathbf{l} = \mathbf{K}_T \cdot \mathbf{x}_{\delta T} = \mathbf{K}_{\alpha:1} \cdot \mathbf{K}_{N:\alpha} \cdot \mathbf{K}_{T:N} \cdot \mathbf{x}_{\delta T} \,. \tag{17}$$

Nonlinearity of the relation of T to N (see Equation (18)) necessitates linearization at this step. The choice of reference state $\mathbf{x}_{0,T}$ does not matter as long as it ensures linearity; that is, values in $\mathbf{x}_{\delta T}$ shall be a factor of 10 or more smaller than those in $\mathbf{x}_T$ (the obvious choice is $\mathbf{x}_{0,T} = \mathbf{x}_{ap,T}$, which certainly ensures $\mathbf{x}_{\delta T,i} < 0.1\mathbf{x}_{T,i}$). Since the linearization well applies, the use of the approximate mapping $\mathbf{K}_{T:N} \cdot \mathbf{x}_{\delta T}$, instead of a rigorous nonlinear mapping $\mathbf{K}_{T:N}(\mathbf{x}_T)$, in no way compromises the validity of the present error analysis and characterization.

In formulating $\mathbf{K}_{T:N}$ it was found convenient to use the inverse operator $\mathbf{K}_{N:T}$ as basic expression and then to obtain $\mathbf{K}_{T:N} = \mathbf{K}_{N:T}^{-1}$ by inversion. We utilized the equation of state (ideal gas law), the standard relation for temperature retrieval in dry air [e.g., *Kursinski et al.*, 1997], in the form

$$\begin{aligned} \frac{p(z)}{\rho(z)} &= \frac{R}{\overline{M}} T(z) \;\Leftrightarrow \\ T(z) = c_1 \frac{p(z)}{N(z)} &= \frac{c_1 k_{N:\rho}}{N(z)} \int_z^\infty g(z) N(z) dz \,, \end{aligned} \tag{18}$$

where again $\rho(z) = k_{N:\rho} \cdot N(z)$ was invoked (introduced in section 4.3 together with the constants R, $\overline{M}$, and c_1), and where Equation (16), rearranged to hydrostatic integral form, was inserted. The actual implementation of $\mathbf{K}_{N:T}$ was based on the operator "**C**" introduced by *Rieder and Kirchengast* [2001, equation (24)] in the context of absorptive occultations for an equation equivalent to (18). A discretization of the hydrostatic integral into layers of varying width is intrinsic in that formulation. A similar formulation was used for the step from N to T by *Syndergaard* [1999]. Matrix inversion then led to the required forward operator $\mathbf{K}_{T:N} = \mathbf{K}_{N:T}^{-1}$, which maps temperature change to refractivity change consistent with both

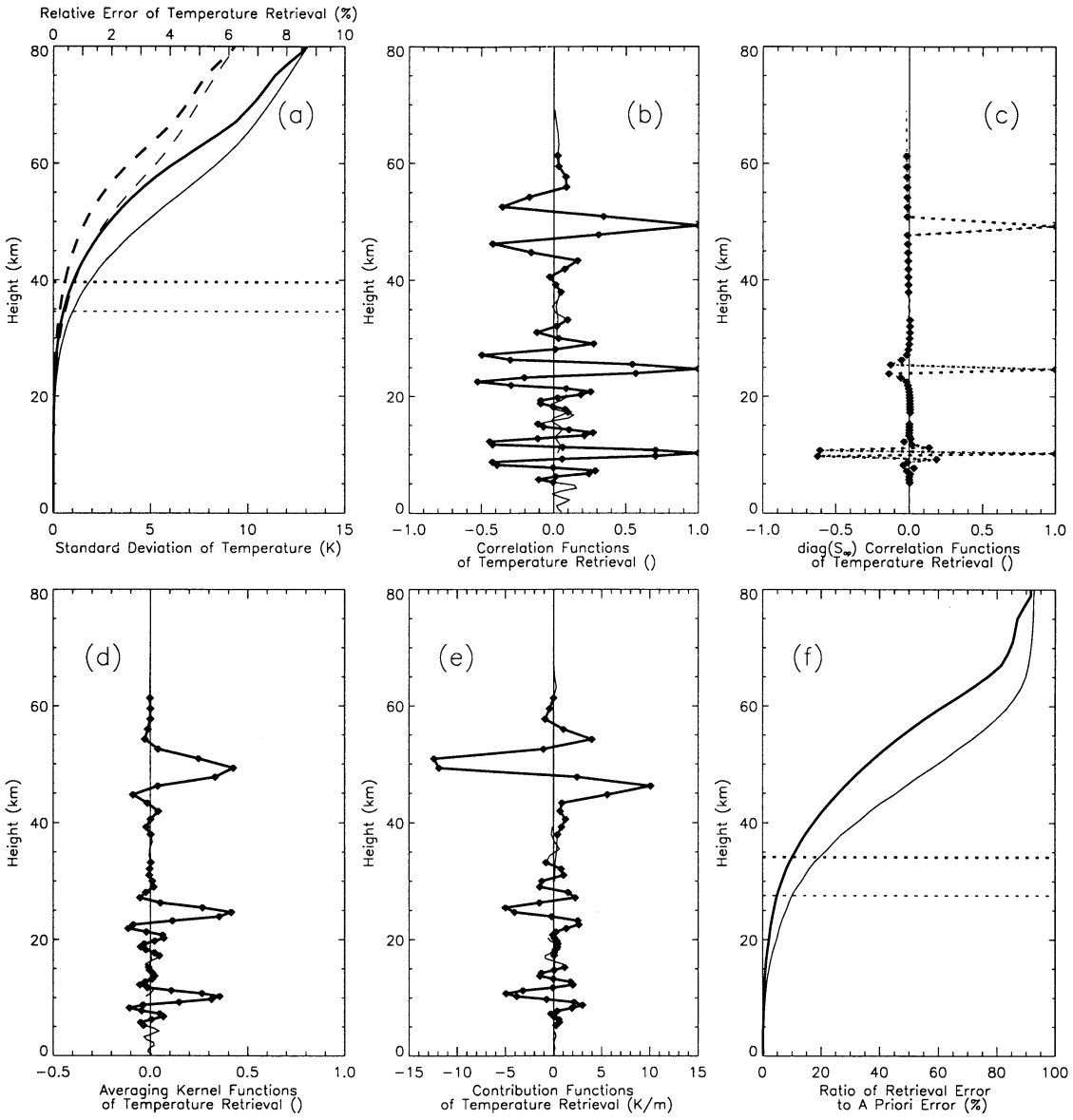

Figure 6. Temperature retrieval results for AR scenario (heavy lines) and SR scenario (light lines, Figures 6a and 6f) given L_σ = 3 km (except Figure 6c, L_σ = 0.5 km). Different from Figure 3, 1 K (rather than 1%) accuracy heights are shown in Figure 6a (dotted horizontal) and the upper two contribution functions in Figure 6e are downscaled by a factor of 100 (the one for ~50 km) and 10 (the one for ~25 km), respectively. Otherwise same format as Figure 3; see Figure 3 caption for description.

the hydrostatic and the ideal gas law. Left-multiplying $\mathbf{K}_{T:N}$ by $\mathbf{K}_N = \mathbf{K}_{\alpha:l} \cdot \mathbf{K}_{N:\alpha}$ finally yields the complete mapping $\mathbf{K}_T$ (see (13) and (17)).

Inserting $\mathbf{K}_T$ together with $\mathbf{S}_\varepsilon$ and $\mathbf{S}_{ap,T}$ formulated in section 4.1 into (3), (7), and (8), we computed covariance matrix $\hat{\mathbf{S}}_T$, characterization matrices $\mathbf{A}_T$ and $\mathbf{D}_T$, and vector $\mathbf{q}_T$, respectively. For both the AR and SR scenarios, Figure 6 illustrates these quantities for the temperature retrieval in the same format as used for Figures 3 to 5 (except that now in Figure 6a the dotted horizontal lines indicate 1 K threshold instead of 1% threshold).

The RMS errors (Figure 6a) are found to be smaller than 1 K below ~40 km/~35 km in the AR/SR scenario (dotted horizontal lines) and to approach a priori values in the mesosphere. These RMS errors due to unbiased phase errors of the magnitude prescribed are fairly reasonable down into the lower stratosphere [e.g., cf., *Kursinski et al.*, 1997]. According to recent results of an ensemble-based empirical error analysis under very realistic conditions (A.K. Steiner and G. Kirchengast, unpublished material, 2001), which involved also bias errors changing from profile to profile (e.g., residual precise orbit determination (POD) errors, ionosphere residual errors), the latter contribute appreciably to the total RMS error above ~25 km. This implies that the total RMS temperature errors of AR-type sensors may be better represented by the SR scenario results at these heights, though the AR scenario well represents the unbiased error component. The recent results also show, in line with the simplified scenario simulations of

Kursinski et al. [1997], that the RMS error level saturates at a minimum level of ~0.2–0.4 K within ~10–20 km and then significantly increases downward because of the presence of moisture. The absence of this behavior at lower stratospheric and tropospheric heights in Figure 6a again points to the role of forward modeling error sources not subsumed into $\mathbf{S}_\varepsilon$ for this baseline analysis. As there is no problem to apply the formalism to any different $\mathbf{S}_\varepsilon$, we plan to run further scenarios with more sophisticated matrices $\mathbf{S}_\varepsilon$ after empirical analyses have better quantified their structure.

The correlation functions and averaging kernel functions (Figures 6b–6d) are found to behave rather similar to their respective refractivity counterparts (Figures 4b–4d); that is, the pronounced pressure error correlations play a small role only in shaping the temperature error correlation structure. This may be surprising at first glance but is not unexpected noting that the operation $\mathbf{K}_{N:T}$ derives T directly from N. It can be more rigorously understood by inspecting the structure of $\mathbf{K}_{N:T}$, as discussed in some detail by *Rieder and Kirchengast* [2001] on the basis of an explicit expression for $\mathbf{K}_{N:T}$.

The contribution functions (Figure 6e) also roughly reflect in shape the contribution functions of refractivity (Figure 4e) but with opposite sign. The reason is that, via (18), temperature is inversely proportional to refractivity, a proportionality only modestly modulated by the hydrostatic integral in the numerator, since the latter contains refractivity in a distinctly nonlocal manner only. The magnitude of the dominating peak of about 2.5/0.1/0.01 K per 2 mm for the function of level ~50/~25/~10 km again agrees well with the unbiased RMS error level (Figure 6a) for the AR scenario (note the rescaling of the upper two functions; see Figure 6 caption). The magnitude is strongly height-dependent, since temperature changes are inversely proportional to mean refractivity, which exponentially decreases with height [see *Rieder and Kirchengast*, 2001, equation (24)]. The retrieval-to-a priori error ratio profiles (Figure 6f) indicate an enhanced role of a priori information for temperature retrievals, compared to previous data products. Ratios <10% are reached at ~34 km/~28 km for the AR/SR scenario, some 10 to 20 km lower than for the other products. This is mainly caused by the comparatively low fractional uncertainty specified in $\mathbf{S}_{ap,T}$ (see section 4.1).

5. Summary and Conclusions

A rigorous error analysis and characterization methodology [*Rodgers*, 1976, 1990, 2000] has been applied to investigate performance properties of atmospheric profiles retrieved from GNSS radio occultation data. Using excess phase measurements as starting point, the processing chain to bending angle, refractivity/density, pressure, and temperature, respectively, was studied in a baseline analysis assuming unbiased measurement errors, spherical symmetry in the occultation tangent point region, and dry air. Low signal-to-noise ratio (SNR) of the measurements at mesospheric altitudes prompted the adoption of a Bayesian approach, which allows one to objectively combine measured data with a priori data and explicitly provides, in the sense of optimal linear unbiased estimation, error covariance matrices for all retrieval products of interest as well as various sensitivity matrices characterizing the retrieval process, including the sensitivity of a retrieved profile to the true profile, the measurements, and the a priori profile. The required inputs are measurement error and a priori error covariance matrices, a priori profiles, and forward operators expressing the physical relations in the retrieval chain, respectively.

After generically summarizing the formalism for the intended purpose, it was applied to GNSS occultation data processing with the required inputs formulated in a reasonable manner. Error analysis and characterization results for the retrieval products bending angle, refractivity/density, pressure, and temperature, respectively, have then been discussed on the basis of two different sensor error scenarios, an advanced receiver (AR) scenario (white Gaussian excess phase noise with 2 mm RMS error at 10 Hz sampling rate) and a standard receiver (SR) scenario (5 mm instead of 2 mm). For each product the discussion utilized the output of the formalism in terms of unbiased RMS error profiles and associated error correlation functions (inspected with and without significant a priori error correlations), averaging kernel functions indicating the sensitivity of retrieved values to the true profile, contribution (or gain) functions indicating the sensitivity of the retrieved profile to the measurements, and retrieval-to-a priori error ratios roughly indicating the influence of the a priori data on the retrieval, respectively. The following main conclusions can be drawn.

1. Below the stratopause down into the lower stratosphere, where the SNR is high, the Bayesian optimal estimation analysis led to RMS error results consistent with previous results based on classical inversion techniques [e.g., *Kursinski et al.*, 1997; *Syndergaard*, 1999], confirming its nominal property to subsum classical approaches in scope.

2. At mesospheric heights, where the SNR is low, the RMS error results of this analysis are significantly more reasonable than previous ones, due to the sensible way of including a priori data.

3. Over the full height range, for both high and low SNR, a robust quantification of the error correlation structure in all retrieval products was obtained, which classical covariance propagation analyses by concept fail to provide under low SNR conditions.

4. At lower stratosphere/troposphere heights the unbiased error level estimates of the scenarios discussed are overly optimistic, since besides bias errors, forward modeling errors [e.g., *Palmer et al.*, 2000] were deliberately not subsumed into the measurement error covariance matrix ($\mathbf{S}_\varepsilon$) for this baseline analysis. As there is no problem to applying the formalism to any different $\mathbf{S}_\varepsilon$, it is planned to run further scenarios with more sophisticated matrices $\mathbf{S}_\varepsilon$ after empirical analyses have better quantified their structure.

5. Beyond any results from previous retrieval chain analyses, quantitative step-by-step insight into the retrieval process was achieved via characterization by sensitivity functions (averaging kernel functions, contribution functions) and retrieval-to-a priori error ratio profiles, representing significant progress toward understanding the chain in full depth. Findings included that the overall magnitude of measurement errors (RMS error level of excess phase profiles) only marginally affects the correlation structure and the sensitivity functions of the retrieval products below the stratopause.

6. The a priori correlation structure importantly influences the correlation structure of the retrieval errors. Similarly, the specific implementation of forward/inverse operators, which

map profiles from one product to the next according to physical relations, significantly influences these correlations. Thus, though the discussed results furnish a good baseline idea, a dedicated error analysis should be performed for each specific processing chain. The formalism proposed here is one excellent candidate for this purpose; a complementary one is ensemble-based empirical error analysis dealt with in a forthcoming paper.

7. According to the retrieval-to-a priori error ratio profiles, a priori information plays a minor role from the upper stratosphere downward (the most appreciable role for temperature), while it starts to dominate in the mesosphere. The influence of the a priori correlation spread reaches significantly further down than the above ratio (a variance-only quantity) indicates, however, since the correlation spread in the data is usually small compared to the one associated with the a priori profile. For keeping correlation structure simple and spread small, it is thus advisable to fuse in a priori data only down to heights where they benefit the processing (>30 km is sufficient from our experience).

8. The formalism intrinsically performs statistical optimization in a rigorous manner by unbiased optimal fusion of measurements with a priori data; a noteworthy aspect given the prominent role played by (approximate) statistical optimization of bending angle profiles in most current retrieval algorithms. Moreover, the correlation structure for the data need not be supplied at retrieval product level but at measurement level only, which is usually more simple.

9. This study, together with a related study by *Rieder and Kirchengast* [2001] on absorptive occultations, introduced convenient (matrix) formulations for relevant forward/inverse operators as well as formulae providing insight into the error propagation process, which will be of significant utility for applications beyond these studies.

In summary, Bayesian optimal estimation was demonstrated to enable a more complete and consistent quantification of properties of profiles retrieved from GNSS occultation data than previous approaches applied. Looking beyond error analysis and characterization, it allows optimal fusion, or "assimilation," of GNSS occultation data not only with single a priori profiles but rather with data from any other suitable (spaceborne) instruments and with atmospheric fields from (dynamical) models.

Acknowledgments. The authors thank U. Foelsche and A.K. Steiner (IGAM, Univ. of Graz, Austria) for many fruitful scientific discussions on the topic and S. Syndergaard (Univ. of Arizona, Tucson, USA) for valuable comments on the manuscript. M.J.R. received financial support for this work from the START research award of G.K. funded by the Austrian Ministry for Education, Science, and Culture and managed under Program Y103-CHE of the Austrian Science Fund. Furthermore, part of the work of M.J.R. was supported by the European Space Agency (ESA/ESTEC, Noordwijk, Netherlands) under Contract 13327/98/NL/GD.

References

Ahmad, B., and G. L. Tyler, Systematic errors in atmospheric profiles obtained from Abelian inversion of radio occultation data: Effects of large-scale horizontal gradients, *J. Geophys. Res.*, *104*, 3971-3992, 1999.

ESA/EUMETSAT, The GRAS instrument on METOP, *ESA/EUMETSAT Rep. (ESA VR/3021/PI, EUMETSAT EPS/MIS/IN/9)*, 38 pp., Noordwijk, Netherlands, 1998.

Eyre, J. R., Assimilation of radio occultation measurements into a numerical weather prediction system, *ECMWF Tech. Memo. 199*, Eur. Cent. for Med. Range Weather Forcasts, Reading, U.K., 1994.

Fjeldbo, G., A. J. Kliore, and V. R. Eshleman, The neutral atmosphere of Venus as studied with the Mariner V radio occultation experiments, *Astron. J.*, *76*, 123-140, 1971.

Fleming, E. L., S. Chandra, M. R. Schoeberl, and J. J. Barnett, Monthly mean global climatology of temperature, wind, geopotential height and pressure for 0–120 km, *NASA Techn. Memo. 100697*, Natl. Aeronaut. and Space Admin., Washington, D. C., 1988.

Gorbunov, M. E., and A. S. Gurvich, Microlab-1 experiment: Multipath effects in the lower troposphere, *J. Geophys. Res.*, *103*, 13,819-13,826, 1998.

Gorbunov, M. E., A. S. Gurvich, and L. Bengtsson, Advanced algorithms of inversion of GPS/MET satellite data and their application to reconstruction of temperature and humidity, *MPIM Rep. 211*, 40 pp., MPI for Meteorol., Hamburg, Germany, 1996.

Healy, S. B., and J. R. Eyre, Retrieving temperature, water vapour and surface pressure information from refractive index profiles derived by radio occultation: A simulation study, *Q. J. R. Meteorol. Soc.*, *126*, 1661-1683, 2000.

Hedin, A. E., Extension of the MSIS thermosphere model into the middle and lower atmosphere, *J. Geophys. Res.*, *96*, 1159-1172, 1991.

Hocke, K., Inversion of GPS meteorology data, *Ann. Geophys.*, *15*, 443-450, 1997.

Hocke, K., G. Kirchengast, and A. K. Steiner, Ionospheric correction and inversion of GNSS occultation data: problems and solutions, *IMG/UoG Tech. Rep. ESA/ESTEC 2/'97*, 35 pp., Inst. for Geophys., Astrophys., and Meteorology, Univ. of Graz, Austria, 1997.

Hoeg, P., A. Hauchecorne, G. Kirchengast, S. Syndergaard, B. Belloul, R. Leitinger, and W. Rothleitner, Derivation of atmospheric properties using a radio occultation technique, *DMI Sci. Rep. 95-4*, 205 pp., Danish Meteorol. Inst., Copenhagen, Denmark, 1995.

Kirchengast, G., J. Hafner, and W. Poetzi, The CIRA86aQ_UoG model: An extension of the CIRA-86 monthly tables including humidity tables and a FORTRAN95 global moist air climatology model, *IMG/UoG Tech. Rep. ESA/ESTEC 8/'99*, 18 pp., Inst. for Geophys., Astrophys., and Meteorology, Univ. of Graz, Austria, 1999.

Kursinski, E. R., et al., Initial results of radio occultation observations of Earth's atmosphere using the global positioning system, *Science*, *271*, 1107-1110, 1996.

Kursinski, E. R., G. A. Hajj, K. R. Hardy, J. T. Schofield, and R. Linfield, Observing Earth's atmosphere with radio occultation measurements using the Global Positioning System, *J. Geophys. Res.*, *102*, 23,429-23,465, 1997.

Ladreiter, H. P., and G. Kirchengast, GPS/GLONASS-sensing of the neutral atmosphere: Model independent correction of ionospheric influences, *Radio Sci.*, *31*, 877-891, 1996.

Melbourne, W. G., E. S. Davis, C. B. Duncan, G. A. Hajj, K. R. Hardy, E. R. Kursinski, T. K. Meehan, L. E. Young, and T. P. Yunck, The application of spaceborne GPS to atmospheric limb sounding and global change monitoring, *JPL Publ. 94-18*, 147 pp., Jet Prop. Lab., Pasadena, Calif., 1994.

Palmer, P. I., J. J. Barnett, J. R. Eyre, and S. B. Healy, A nonlinear optimal estimation inverse method for radio occultation measurements of temperature, humidity, and surface pressure, *J. Geophys. Res.*, *105*, 17,513-17,526, 2000.

Rieder, M. J., and G. Kirchengast, Error analysis for mesospheric temperature profiling by absorptive occultation sensors, *Ann. Geophys.*, *19*, 71-81, 2001.

Rocken, C., et al., Analysis and validation of GPS/MET data in the neutral atmosphere, *J. Geophys. Res.*, *102*, 29,849-29,866, 1997.

Rodgers, C. D., Retrieval of atmospheric temperature and

composition from remote measurements of thermal radiation, *Rev. Geophys., 14*, 609-624, 1976.

Rodgers, C. D., Characterization and error analysis of profiles retrieved from remote sounding measurements, *J. Geophys. Res., 95*, 5587-5595, 1990.

Rodgers, C. D., *Inverse Methods for Atmospheric Sounding: Theory and Practice*, 256 pp., World Sci., River Edge, N.J., 2000.

Salby, M. L., *Fundamentals of Atmospheric Physics*, 627 pp., Academic P., San Diego, Calif., 1996.

Sokolovskiy, S. V., and D. Hunt, Statistical optimization approach for GPS/MET data inversions, paper presented at 2nd URSI GPS/MET Workshop, Int. Union of Radio Science, Tucson, Ariz., Feb. 1996.

Steiner, A. K., G. Kirchengast, and H. P. Ladreiter, Inversion, error analysis, and validation of GPS/MET occultation data, *Ann. Geophys., 17*, 122-138, 1999.

Syndergaard, S., Retrieval analysis and methodologies in atmospheric limb sounding using the GNSS radio occultation technique, *DMI Sci. Rep. 99-6*, 131 pp., Danish Meteorol. Inst., Copenhagen, Denmark, 1999.

Vorob'ev, V. V., and T. G. Krasil'nikova, Estimation of the accuracy of the atmospheric refractive index recovery from Doppler shift measurements at frequencies used in the NAVSTAR system, *Phys. Atmos. Oceans, 29*, 602-609, 1994.

Ware, R., et al., GPS sounding of the atmosphere from low Earth orbit–Preliminary results, *Bull. Am. Meteorol. Soc., 77,* 19-40, 1996.

M. J. Rieder and G. Kirchengast, Institute for Geophysics, Astrophysics, and Meteorology (IGAM), University of Graz, Universitaetsplatz 5, A-8010, Graz, Austria. (markus.rieder@uni-graz.at; gottfried.kirchengast@uni-graz.at)

(Received October 17, 2000; revised June 18, 2001;
accepted June 18, 2001.)